N.B.: This is the ACCEPTED version of this article. The final, published version of the article can be found at: https://doi.org/10.1016/j.enconman.2021.115016

Techno-economic analysis of recuperated Joule-Brayton pumped thermal energy storage

Joshua D. McTigue[a,*], Pau Farres-Antunez[b], Kavin Sundarnath Jawaharlal Ayyanathan[c], Christos N. Markides[d], Alexander J. White[b]

[a] *National Renewable Energy Laboratory, 15013 Denver West Parkway, Golden, Colorado, 80401, USA*
[b] *Cambridge University Engineering Department, Trumpington Street, Cambridge, CB2 1PZ, UK*
[c] *New Mexico State University, New Mexico, USA*
[d] *Clean Energy Processes (CEP) Laboratory, Department of Chemical Engineering, Imperial College London, London SW7 2AZ, UK*

Abstract

This article describes a techno-economic model for pumped thermal energy storage systems based on recuperated Joule-Brayton cycles and two-tank liquid storage. Models have been developed for each component, with particular emphasis on the heat exchangers. Economic metrics such as the power and energy capital costs (i.e., per-kW and per-kWh capacity) and levelized cost of storage are evaluated by gathering numerous cost correlations from the literature, thereby enabling estimates of uncertainty. It is found that the use of heat exchangers with effectivenesses up to 0.95 is economically worthwhile, but higher values lead to rapidly escalating component size and system cost. Several hot storage fluids are considered; those operating at the highest temperatures (chloride salts) improve the round-trip efficiency but the benefit is marginal and may not warrant the additional material costs and risk when compared to lower-temperature nitrate salts. Cost-efficiency trade-offs are explored using a multi-objective optimization algorithm, yielding optimal designs with round-trip efficiencies in the range 59-72% and corresponding levelized storage costs of 0.12±0.03 and 0.38±0.10 \$/kWh$_e$. Lifetime costs are competitive with lithium-ion batteries for discharging durations greater than 6 hours under current scenarios.

Keywords: energy storage, heat pump, pumped thermal energy storage, Carnot battery, molten salt

*Corresponding author
Email address: jmctigue_nrel@outlook.com (Joshua D. McTigue)

Nomenclature

Abbreviations

CAES	Compressed air energy storage
COP	Coefficient of performance
CSP	Concentrating solar power
FCR	Fixed charge rate
HX	Heat exchanger
LAES	Liquid air energy storage
LCOS	Levelized cost of storage, \$/kWh$_e$
LiB	Lithium-ion battery
O&M	Operation and maintenance costs 2020 USD/year
PHES	Pumped heat energy storage
PTES	Pumped thermal energy storage
SEPT	Stockage d'électricité par pompage thermique
SMES	Superconducting magnetic energy storage
TMES	Thermo-mechanical energy storage

Greek symbols

β	Pressure ratio
η_{HE}	Heat engine efficiency
$\eta_{m,g}$	Motor or generator efficiency
$\eta_{p,i}$	Polytropic or isentropic efficiency
η_{RT}	Round-trip efficiency
ρ	Density, kg/m^3
ρ_E	Energy density, kWh$_e$/m^3
$\tau_{\mathrm{chg,dis}}$	Charge/discharge duration, s
ε	Heat exchanger effectiveness

Roman symbols

$\bar{c}_{\mathrm{en}}$	Specific cost of energy storage components, 2020 USD/kWh$_e$

$\bar{c}_{\mathrm{pow}}$	Specific cost of power components, 2020 USD/kW$_{\mathrm{e}}$
$\dot{m}$	Mass flow rate, kg/s
$\dot{Q}$	Heat, W
$\dot{W}$	Power, W
Nu	Nusselt number
Re	Reynolds number
A	Heat transfer area, m^2
A_{f}	Flow area, m^2
C	Cost, 2020 USD
C_{en}	Total cost per unit energy output, 2020 USD/kWh$_{\mathrm{e}}$
c_{f}	Friction coefficient
C_{pow}	Total cost per unit power output, 2020 USD/kW$_{\mathrm{e}}$
c_p	Specific heat capacity, J/kg.K
D	Hydraulic diameter, m
E	Energy, J
f_p	Fractional pressure loss
G	Mass flux, kg/m^2.s
h	Enthalpy, J/kg
h_{t}	Heat transfer coefficient, W/m^2.K
k	Thermal conductivity, W/m.K
L	Heat exchanger length, m
N_{cyc}	Number of charge and discharge cycles per year
p	Pressure, Pa
P_{el}	Price of electricity, 2020 USD/kWh$_{\mathrm{e}}$
R	Work ratio
T	Temperature, K
U	Overall heat transfer coefficient, W/m^2.K
V	Volume, m^3

1. Introduction

Renewable generation currently supplies about 11% of global electricity demand [1]. This fraction is set to rise and efforts to electrify the transport and heating sectors (which together constitute 83% of global energy consumption) are likely to further accelerate the uptake of renewables. Recent reports indicate that wind and photovoltaic electricity are now cheaper than new-build fossil-fuel generation on a per-unit-energy (levelized-cost) basis, and are cost-competitive with existing conventional plants [2]. However, it is often argued that the intermittent and non-dispatchable nature of the renewable technologies (especially wind and solar) will require additional measures to ensure grid stability and security of supply. These are likely to incur additional system costs and it is perhaps therefore misleading to consider per-unit-energy costs of a particular generating technology in isolation. Finding cost-effective ways of balancing the grid with high penetrations of wind, solar and other renewables is thus an important, ongoing research topic.

Methods for facilitating further integration of renewables include expansion of grid interconnections [3], demand-side management (e.g., flexible use of electric vehicle batteries [4]), over-sizing renewable capacity, fossil- and bio-fuel peaking plants, and energy storage. The extent to which each of these will contribute to mitigating intermittency and non-dispatchability remains a matter of speculation. As far as storage is concerned, many different systems exist or have been proposed, ranging from established technologies such as pumped-hydro storage and electro-chemical batteries to emerging technologies, such as flow batteries [5] and thermo-mechanical energy storage (TMES) systems (which includes compressed air energy storage (CAES) and liquid air energy storage (LAES) [6]), to those technologies that are in their infancy, such as superconducting magnetic energy storage (SMES) [7]. A review of these technologies is given in Ref. [8] which compares their key performance indicators and describe their state of development and target applications.

1.1. Overview of pumped thermal energy storage

The present article is concerned with a form of TMES system known as pumped thermal energy storage (PTES). This terminology refers to any storage system that uses an electrically-driven heat pump during its charge phase to deliver heat to a hot store and/or extract heat from a cold store, and a heat engine to retrieve electrical work during discharge. PTES may be considered as a subset of the Carnot Battery category of storage, which also includes systems that use resistive heating to charge the hot store [9]. As with all storage technologies, the round-trip efficiency (η_{RT}) of PTES is limited only by irreversibilities: a (fictitious) reversible system would have an η_{RT} of 100%, but with realistic component efficiencies projected values are in the range 40-70% [10].

In common with many TMES systems, the energy and power capacities of PTES can be decoupled and, in particular, the marginal cost of additional energy storage is potentially very low. It is therefore well-suited to longer-duration discharge requirements, such as those caused by wind lulls. As discussed in Ref. [11], most recent energy storage deployments have been short duration operating reserves, but it is expected that new storage deployments will have increasing discharge durations. Storage will initially provide peaking capacity and arbitrage with discharging durations of 2-6h, as is being observed with lithium-ion batteries (LiB). The deployment of these technologies will increase the length of net load peaks [11], requiring the deployment of longer-duration storage (>4h) which may also be able to provide additional sources of value, such as transmission deferral. To provide longer duration storage, these technologies must be cost-competitive with LiBs to be viable, and in particular, should have low marginal costs of energy storage capacity. This article conducts techno-economic analysis to investigate the costs required to achieve a transition from LiBs to PTES, and the discharging duration at which lifetime cost parity is reached.

Concepts similar to PTES can be traced back almost a century and include Maguerre's proposal for energy storage in steam accumulators [12] and Weissenbach's open gas turbine cycle with thermal storage [13]. Most developments have occurred in the past two decades and early work (initiated pre-2010) includes the French SEPT system (le stockage d'électricité par pompage thermique – which translates almost exactly as PTES) [14] and Isentropic Ltd.'s PHES (pumped heat energy storage) in the UK [15]. Both of these are based on the Joule-Brayton cycle and exploit packed beds of gravel (or similar) as the storage medium [16]. Gravel stores can be charged and discharged efficiently [17] and is cheap, abundant and can operate over a wide temperature range. But a major drawback is that such stores need to be pressurized, adding substantially to the specific (per-kWh) capital cost [18]. In addition, the thermal gradients (thermoclines) that develop along the length of the store have to be carefully managed to avoid compromising the performance of the store [19] or other components in the cycle [20].

These challenges can be avoided by using liquid storage, as first proposed in Ref. [21], which necessitates modifications to the power cycle layout, such as the inclusion of a recuperator [22]. The characteristics of several suitable fluids are summarized in Ref. [23] and a solution using nitrate molten salts is currently being developed commercially by Malta Inc. who are aiming for deployment by 2023 [24]. Recent research has investigated sources of exergy losses within this system [25], and the present work aims to improve the design by also considering the lifetime cost. The use of liquid stores has the advantage that, although not necessary, the working fluid may be pressurized, thereby increasing power density and reducing per-kW capital cost. Two-tank systems are usually proposed, similar to those used in the concentrating solar power (CSP) industry, but single-tank storage is also possible [8]. Previous analyses of PTES indicate that maximum temperatures should be increased to improve the round-trip efficiency [26]. However, higher temperature systems require more expensive materials and components, and this trade-off is explored in this article by considering several different hot storage fluids. Potential hot-storage fluids include mineral and synthetic oils (with top temperatures of around 300°C and 400°C respectively) and nitrate molten salts [25], which typically operate in the range $250 - 565$°C, the lower limit being required to prevent freezing. Substantial experience has been gained in the use of molten salt storage via the CSP industry. Systems based on the Joule-Brayton cycle also require a cold store and finding suitable cold-storage fluids has proved more challenging, as discussed below.

A closed Joule-Brayton cycle integrated with liquid storage has several interesting properties – notably, the result that part-load charging and discharging may occur without appreciably affecting the round-trip efficiency [23]. Typically, these systems use different turbomachines for the charge and discharge phases, whereas the same heat exchangers are used at all times. As a result, the extent to which certain parameters can differ between charge and discharge depends on the components that are affected by those parameters. For example, this configuration allows the discharging pressure ratio to differ from the charging pressure ratio in order to minimize heat rejection. On the other hand, changing the relative duration of charge or discharge affects the mass flow rates through the heat exchangers and therefore the efficiency and cost. The impact of such considerations is explored in this article for the first time.

PTES systems based on a variety of other thermodynamic cycles have been studied, including Rankine [27], trans-critical [28] and Kalina cycles [29], and a combined-cycle PTES-LAES arrangement that obviates the need for the so-called 'cold box' of LAES systems [30]. A review of these and other concepts is provided in Ref. [8], together with appropriate storage media in each case.

1.2. Aims of this study

This study has three objectives: firstly, to develop and describe state-of-the-art models that improve performance and cost estimates of PTES with two-tank liquid storage; secondly, to explore numerous design parameters and optimize the design; finally, to demonstrate its competitiveness by comparing the costs with lithium-ion batteries.

In this article, detailed heat exchanger models are described and validated against experimental data – these components have the greatest influence on efficiency and cost. These models capture variable fluid properties and calculate the geometry, which is important for evaluating the cost and off-design behaviour (the charging and discharging operating conditions are not identical). Auxiliary components such as pumps, fans, motors, and generators, which have a non-negligible impact on performance and cost, are also included. Exergy losses within each component are calculated which reveals the relative importance of each component. These models are described in Section 3 and the Appendix.

A method of evaluating the cost is proposed, which uses a Monte-Carlo method to construct probability distributions of the life-time cost (levelized cost of storage), thereby allowing an assessment of the uncertainty. This method is described in Section 3.6 and further details are provided in the Supplementary Information.

With this techno-economic methodology, several design parameters are investigated. While the influence of heat exchanger design is fairly straightforward, other parameters, such as the discharging pressure ratio, choice of maximum temperature, or relative duration of charge and discharge, have a less obvious impact on system performance and cost. These design choices and trade-offs are explored in Section 5.

A multi-objective optimization method is described in Section 6.1. This technique is used to explore the space of optimal designs, and reveals how best to negotiate the trade-offs described in Section 5. Finally, one of the optimal designs is compared with with lithium-ion batteries (LiB) in Section 6.2 with the aim of dertermining the discharging duration at which PTES becomes economically competitive with LiBs. This analysis also identifies which PTES components provide the greatest scope for cost improvements.

The techno-economic methodology described in this article could be applied to other TMES systems, and enable fair comparisons of various devices.

2. System description and layout

The Joule-Brayton (or gas-turbine) cycle comprises two adiabatic and two isobaric processes and uses an ideal gas as the working fluid. A simplified (reversible) representation on the temperature-entropy diagram is shown in Fig. 1 (left-hand cycle). The cycle is traversed in the anticlockwise sense during the charge (heat-pump) phase and clockwise during the discharge (heat-engine) phase. Thus, for example, the charge process comprises: adiabatic compression (States 1 to 2), isobaric heat rejection to the hot store (2 to 3), adiabatic expansion (3 to 4) and isobaric heat absorption from the cold store (4 to 1). In practice, the charge and discharge cycles are not coincident, due chiefly to thermodynamic irreversibilities during the compression and expansion processes. The temperatures shown in the figure are approximately representative of Isentropic's PHES system, which uses argon as the working fluid and a pressure ratio of ~ 10 [31].

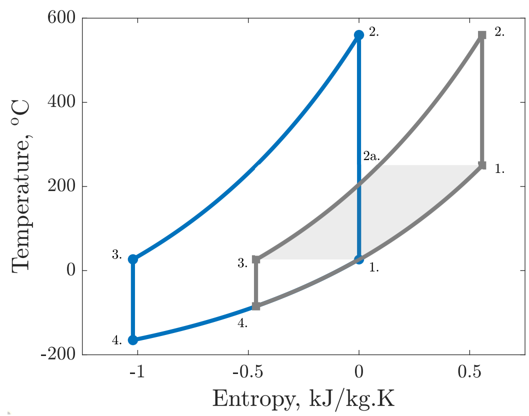

Figure 1: Temperature-entropy diagram of reversible Joule-Brayton cycles. Left (blue): simple cycle; right (grey): recuperated cycle (shading indicates recuperative heat transfer).

If molten salts are used for the hot storage in this cycle, then T_3 must be kept above the salt's freezing point. Although this is feasible with a simple Joule-Brayton cycle the turbine work output (during charge) then becomes a relatively high fraction of the compression work (i.e., the cycle has a poor 'work ratio'), resulting in round-trip efficiencies of $\sim$ 35%, as shown in Ref. [32]. The solution (see for example Laughlin [33]) is to add a recuperating heat exchanger to transfer heat between the high- and low-pressure streams of the working fluid. The typical layout for such a system is shown in Fig. 2 and the effect on the T-s diagram is shown in the right-hand cycle of Fig. 1. Of particular note, the lowest (discharged) temperature of the hot store is now $T_{2a} \sim T_1$, above the salt freezing point, but the work ratio (given approximately by T_2/T_3) is unchanged.

Recuperation also has the benefit of reducing the pressure ratio, which not only reduces the number of compressor and turbine stages but also raises the coldest temperature T_4, thereby permitting a wider choice of cold-storage fluids. In passing, it is interesting to note that the SEPT system described by Desrues *et al* [14] is effectively a recuperated cycle wherein the recuperation is achieved by partial overlap of the hot and cold storage temperature ranges, thus avoiding the need for a separate heat exchanger.

Several hot-storage fluids are considered in the present study, but methanol is used throughout for the cold store. For the reasons outlined above, recuperation is always used so that the layout is as shown in Fig. 2. Note that a 'heat rejection' heat exchanger is required (States 3a to 3 in Fig. 2) to counter the effects of irreversibility. A separate set of compressors and turbines is used for the charge and discharge phases (since these operate at very different inlet temperatures) but the motor-generator and all heat exchangers are common to both phases. The working fluid is pressurized nitrogen gas, this being a compromise between good heat transfer properties (for which lighter gases are better [34]) and ease of compression / expansion (for which lighter gases would require many stages).

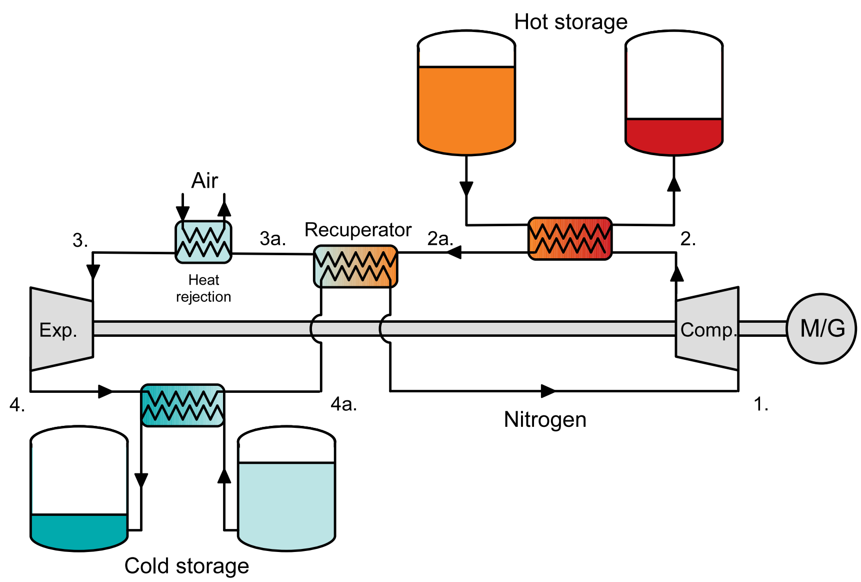

Figure 2: Schematic of a recuperated Joule-Brayton PTES cycle shown during charge.

3. Modelling methods

The overall system model combines standard thermodynamic cycle calculations with a range of cost correlations for the individual components. First it is necessary to specify the working fluid, storage fluids, operating conditions (such as T_1, T_2, p_1) and component performance (such as polytropic efficiency and effectiveness). The cycle state points are then calculated according to these inputs. The discharging power output and duration are specified and from this the mass flow rates, heat exchanger geometry, and storage tank size is calculated. The cycle state points are then re-evaluated for the calculated heat exchanger geometry as described in more detail in Section 3.1 and Appendix A – this is necessary because the charging and discharging cycles differ slightly. Having established the size of each component, the costs are then evaluated using a selection of correlations from the literature. Finally, the lifetime cost is calculated for a set of given financial parameters, see Section 3.6.

Aside from the turbomachinery, heat exchangers and tanks, other components not shown in the layout of Fig. 2 are also modelled, including the motor-generator and auxiliary systems such as fans and pumps. Together these typically incur a 3-5% efficiency penalty and contribute $\sim 10\%$ to the capital cost.

3.1. Heat exchangers

The performance of the systems considered here is strongly dependent on the design of the heat exchangers, due to the high heat-to-work ratio (i.e, ratio of total heat exchange to net work transfer) [23]. Heat exchangers are initially characterized by design values of effectiveness ($\varepsilon = \dot{Q}/\dot{Q}_{\max}$) and fractional pressure loss ($f_p = \Delta p/p_{\text{in}}$). All heat exchangers are assumed balanced (i.e., with equal $\dot{m}c_p$ for the two streams) so as to minimize heat transfer irreversibility [35]. A 'first run' of the full thermodynamic cycle (charge and discharge) is performed using the target values of ε and f_p, in order to obtain approximate operating conditions throughout the cycle. Heat exchanger geometries are then computed so as to meet these target values under the conditions obtained. Since conditions between charge and discharge can vary, the heat exchangers are designed for the period with the highest mass flow rate (i.e., the most stringent conditions, meaning that the device will outperform the design objectives when operating at lower mass flow rates).

The sizing procedure used to compute the heat exchanger geometries is detailed in Appendix A.1. The resulting geometries are used on a second run of the full cycle in which accurate operating conditions are obtained, and for generating economic estimates. The second run is an off-design simulation because, as noted above, operating conditions will generally differ between charge and discharge. (Part-load operation is also important when considering real load cycles). The off-design model employed for this is described in Appendix A.2. Both the sizing procedure and the off-design model are adaptations of common approaches used to model counter-flow heat exchangers in one dimension (see e.g. Refs. [36]). Appendix A provides further details on the algorithms used, including flow diagrams and a validation study.

3.2. Machinery

Compressors and expanders are assumed to be turbomachines and are modelled with a polytropic efficiency, η_p, defined in the usual fashion [37]. For example, for a compression process, the infinitesimal specific work input is given by $dw = dp/(\eta_p \rho)$. For *perfect* gases, this leads to

$$\tau_c = \beta_c^{\phi} \tag{1}$$

where τ_c and β_c are the compressor temperature and pressure ratios respectively, and $\phi = (\gamma - 1)/(\gamma \eta_p)$. Similar relationships hold for expansion processes. For semi-perfect and non-ideal gases – e.g., N_2 at high pressure – the expression for dw needs to be integrated numerically.

The work input to the air fans is also calculated using a polytropic efficiency combined with the fan pressure ratio, $p_2/p_1 = 1/(1 - f_p)$ (where f_p is the pressure loss factor on the air side of the heat-rejecting coolers). However, pump work for the storage fluids is computed from an isentropic efficiency, η_i, assuming the fluid is incompressible. Thus,

$$\dot{W}_{\text{pump}} = \frac{\dot{m} \Delta p}{\rho \eta_i} \tag{2}$$

Finally, the motor-generator (which is a single device) is assumed to be a permanent magnet synchronous machine, and has a design efficiency of approximately 98%. Since the charging and discharging powers will in general differ, the motor-generator will operate off design for at least some of the time. Part-load behaviour is obtained from Ref. [38], which shows significant departure from design-point efficiency only when the the load falls below 50% of its nominal value. Pumps and fans are also driven by motors which are assumed to have efficiencies of 98%.

3.3. Fluid properties

Several fluids are used in the system, including the working fluid, heat-rejection fluid (air), and storage fluids. Thermal properties of the working fluid and ambient air are obtained from CoolProp [39]. Several hot storage fluids are considered including nitrate molten salts, chloride molten salts, synthetic oils and mineral oils. These fluids have different operating temperature ranges, and therefore have a substantial impact on performance. Data for nitrate molten salts, mineral oils and synthetic fluids (namely a biphenyl/diphenyl-oxide mixture such as Therminol VP-1) are obtained from manufacturers' data sheets, and typically include information such as the variation of heat capacity, thermal conductivity, density, and viscosity with temperature. The enthalpy and entropy are then calculated and the data tables are interpolated to find the required properties. Chloride molten salt mixtures can operate at higher maximum temperatures than nitrate molten salts, and a ternary mixture of sodium chloride, potassium chloride, and magnesium chloride is considered here [40]. The cold storage fluid is methanol which may operate at low temperatures and properties are obtained from CoolProp. This fluid is flammable and toxic and therefore an alternative cold storage system may be required.

3.4. Thermal storage

Double tanks are used for both hot and cold storage, so the system has four tanks in total, as shown in Fig. 2. For a given power output during discharge the mass flow rate of working fluid is calculated. The heat exchanger sizing procedure is used to find the storage fluid mass flow rates, from which the total storage fluid volume is calculated. The internal volume of each tank is then oversized by 10%. The tanks are assumed to be internally insulated, and the insulation thickness is calculated assuming a 0.5% energy loss per day following the methodology in Ref. [41]. These energy losses are neglected when calculating the round-trip efficiency since the values are small and the assumed charging and discharging cycles are somewhat shorter than a day.

Other exergetic losses that occur in the tanks are known here as 'cyclic losses': Mixing losses may occur if fluid is already in the tank, and new fluid is introduced at a different temperature. While the total energy is conserved, entropy is generated and corresponds to an exergy loss. Furthermore, an exergy loss occurs if the tank fluid at the end of discharge is a different temperature to the start of charge. For instance, the hot storage fluid may end up hotter than its initial (cool) state at the end of discharge. Heat must therefore be rejected at above-ambient temperatures to ensure cyclic operation, thereby incurring a further exergetic loss.

3.5. Definition of performance metrics

The models above are used to calculate the total electrical work input and output to the cycle, and subsequently metrics such as the round-trip efficiency and energy density. The electrical work is found by accounting for the work into/out of the thermodynamic cycles, the parasitic work input due to pumping and fan work, and the motor-generator efficiency. Although it is possible to ascribe separate second-law efficiencies to charge and discharge, this is not necessary for the current purposes and only the overall round-trip efficiency is considered here. This is given by the fraction of input energy that is extracted from the storage:

$$\eta_{\mathrm{RT}} = \frac{W_{\mathrm{net}}^{d}}{W_{\mathrm{net}}^{c}} = \frac{\eta_g (W_{\mathrm{exp}}^{d} - W_{\mathrm{comp}}^{d}) - (W_{\mathrm{pump}}^{d} + W_{\mathrm{fan}}^{d})/\eta_m}{(W_{\mathrm{comp}}^{c} - W_{\mathrm{exp}}^{c} + W_{\mathrm{pump}}^{c} + W_{\mathrm{fan}}^{c})/\eta_m} \tag{3}$$

where η_m is the motor efficiency, η_g is the generator efficiency, W_{comp} is the compressor work, W_{exp} is the expander work, W_{pump} is the pumping work input, W_{fan} is the fan work, and superscripts c, d represent charge and discharge, respectively.

The energy density (strictly, the exergy density) evaluates the energy per unit volume and provides a guide to the system size (and hence cost). Here, the energy density is defined as the total *electrical* energy dispatched from the system as a fraction of the total system volume which includes all four storage tanks, such that

$$\rho_E = \frac{W^d_{\mathrm{net}}}{V_{\mathrm{tot}}} = \frac{\eta_g (W^d_{\mathrm{exp}} - W^d_{\mathrm{comp}}) - (W^d_{\mathrm{pump}} + W^d_{\mathrm{fan}})/\eta_m}{V_{\mathrm{hot}} + V_{\mathrm{cold}}} \tag{4}$$

where V_{hot} and V_{cold} are the volumes of the four hot and cold storage tanks.

3.6. Economics

The primary economic metrics of interest here are the capital cost and lifetime cost of the system. Evaluating these metrics requires numerous assumptions and estimations. To account for this uncertainty, a Monte Carlo sampling method is used to develop probability distributions of the cost.

The capital cost is found by summing the cost of each component, and then multiplying by a factor that captures installation and contingency costs, such that:

$$C_{\mathrm{cap}} = f_{\mathrm{install}} \sum_i C_i \tag{5}$$

In this analysis, the factor f_{install} is assumed to be in the range of 1.1 to 1.5 [42].

Dividing the total capital cost by the discharged power and discharged energy facilitates comparison between designs and technologies. In this article, these terms are defined as the total cost per unit energy/power *dispatched* during discharge, such that

$$C_{\mathrm{pow}} = \frac{C_{\mathrm{cap}}}{\dot{W}^d_{\mathrm{net}}} \tag{6}$$

$$C_{\mathrm{en}} = \frac{C_{\mathrm{cap}}}{\dot{W}^d_{\mathrm{net}} \tau^d} \tag{7}$$

where τ^d is the discharging duration. These metrics therefore capture the capital cost as a function of the power and energy that are actually delivered as the end product of the storage system. (Capital cost per unit energy/power *capacity* do not capture the fact that the energy storage may not be operated between state-of-charge of 0% and 100%. For instance, a battery might be operated between 10% and 90%, and providing a required energy output will incur a cost 1.25 times greater than the cost per unit energy capacity).

The levelized cost of storage (LCOS) accounts for the lifetime cost of the energy storage system and is evaluated using the 'fixed charge rate' method [43]. The LCOS is expressed as

$$\mathrm{LCOS} = \frac{\mathrm{FCR} \cdot C_{\mathrm{cap}} + \mathrm{O\&M} + E_{\mathrm{in}} P_{\mathrm{el}}}{E_{\mathrm{out}}} \tag{8}$$

where FCR is the fixed charge rate, C_{cap} is the capital cost, O&M is the annual operations and maintenance cost, E_{in} is the annual electrical energy purchased from the grid, P_{el} is the average electricity price, and E_{out} is the annual electrical energy discharged from the storage. The fixed charge rate incorporates data such as the projected lifetime of the plant and the discount rate, as detailed in the Supplementary Information. The lifetime is assumed to be 25-35 years, the electricity price is 0.025-0.06 \$/kWh$_{\mathrm{e}}$, and the operations and maintenance cost is 1-5% of the total capital cost [44]. (Note that ranges are given here, because these uncertain variables are also factored into a Monte Carlo uncertainty calculation, described below). It is assumed that the system charges and discharges once per day, and therefore undergoes 365 cycles per year. The cycles are assumed to occur at the design point so that $E_{\mathrm{out}} = \eta_{\mathrm{RT}} E_{\mathrm{in}}$. Thus, the LCOS accounts for both the economic cost and the efficiency of the storage system. The LCOS is a somewhat limited metric as it only accounts for the cost of the system, and not the value and revenue that it provides. Furthermore, energy storage systems are likely to have more complicated load cycles that respond to the requirements of the grid. However, these factors are dependent on the location and application and introduce many more variables and uncertainties. The simple LCOS method described here is sufficient to enable comparison between PTES designs and to compare with other storage technologies.

Following an approach similar to those used in Ref. [44], component costs have been obtained from a range of correlations for each component available in the literature. These are often based on vendor data but can vary by a factor of up to 100 for the same component, thereby leading to significant uncertainty. A Monte Carlo method is therefore used to calculate probability distributions for the overall system capital cost. Component sizing is first undertaken (following the thermodynamic cycle calculations described above) which enables each component to be costed as described below. Total system cost is then computed by combining a random permutation of component correlations. This process is repeated thousands of times to generate relatively smooth distributions from which mean cost, standard deviation and confidence intervals can be extracted. An sample calculation is given in the Supplementary Information. Precise details of all the cost correlations are also provided in the Supplementary Information, but the main features may be summarized as follows:

(i) Compressors and expanders: Costs typically depend on power rating but may alternatively be expressed in terms of the mass flow and pressure ratio. A relationship of the form $C \propto \dot{W}^n$ is generally accepted, with n typically in the range 0.6 to 0.8 but in some cases $n = 1$ (linear dependence). Correlations for turbomachinery may include a temperature-dependent factor to reflect the increased complexity and materials requirements for high-temperature operation. Many of the correlations have been developed for open-cycle gas turbines but may be modified to treat pressurized closed-cycle operation by scaling inversely with fluid density to reflect the smaller machine size.

(ii) Heat exchangers: Cost relations normally take the form $C \propto A^n$ where A is the heat-transfer area and n is typically 0.6. Additional factors may be included to account for pressure rating, material and heat exchanger type (which in the present study is limited to shell-and-tube). The temperature-dependent materials cost multipliers are summarized in Table 1. It is notable that they militate strongly against high-temperature storage.

(iii) Storage: Tank costs also follow a power law based on either weight or volume, with $n \sim 0.6$. All tanks are at ambient pressure and are assumed internally insulated so as to allow construction from carbon steel. No temperature or pressure-dependent factors are therefore required. Insulation thickness is calculated so as to limit the drop in temperature difference (from ambient) to 0.5% per day. Insulation and storage-fluid costs are readily determined on the basis of mass or volume.

Table 1: Heat exchanger material cost factors

Temperature, °C	Material	Cost factor
T $\leq$ 400	carbon steel	1
$400 < T \leq 600$	stainless steel	2
T $>$ 600	nickel alloy	5

4. Results: Nominal design

A nominal design case is introduced to illustrate the typical performance and cost of PTES. The nominal PTES design is a large electricity storage system, and has a discharging power output of 100 MW_e for a duration of 10 hours – i.e., a 1000 MWh_e system. The charging and discharging durations are equal, which implies that the charging power rating is larger than the discharging power. (Different charging power inputs are investigated in Section 5.4). The system uses nitrate molten salts for the hot storage and is limited to a maximum storage temperature of 565 °C. Temperature-entropy diagrams for the charging and discharging cycles are shown in Fig. 3. Other parameters and corresponding results are shown in Table 2. Input parameters of interest are subsequently varied while keeping the other parameters fixed at their nominal values.

Table 2: Design and performance of the nominal PTES design

Nominal case design		
Discharging power	MW_e	100
Discharging duration	h	10
Charging duration	h	10
Ambient temperature	°C	25
HX effectiveness	-	0.95
HX pressure loss	%	1
Polytropic efficiency	%	90
Motor/generator efficiency	%	98
Maximum pressure	bar	25
Discharge pressure ratio		Same as charge
Working fluid		Nitrogen
Hot storage fluid		Nitrate molten salt
Cold storage fluid		Methanol
Nominal case performance		
COP	-	1.3
Heat engine efficiency	%	45
Round-trip efficiency	%	53
Energy density	kWh_e/m^3	15
Capital cost	M$	260 ± 73
Cost per unit power	$\$/kW_e$	2600 ± 700
Cost per unit energy	$\$/kWh_e$	260 ± 70
Levelized cost of storage	$\$/kWh_e$	0.13 ± 0.03

Under these conditions, the round-trip efficiency is 53% and the majority of available work is lost in the compressors, expanders, and heat exchangers. The distribution of exergy losses is shown in Fig. 4. Parasitic losses due to pumping, fanning, and motor-generator inefficiency account for several percentage points of lost work and indicates the importance of including these components in system

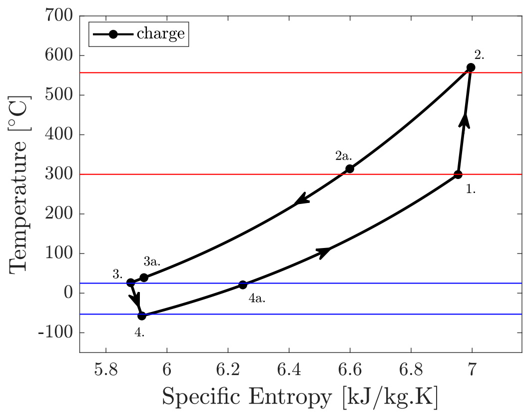

(a)

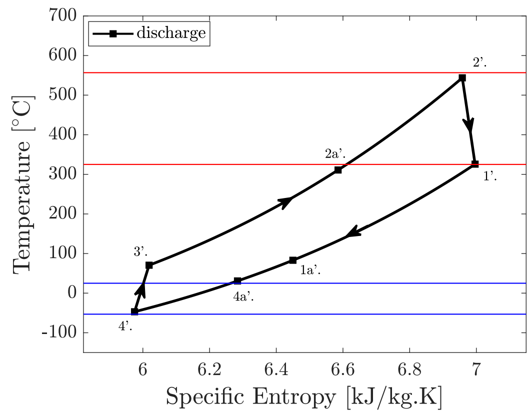

(b)

Figure 3: Temperature-entropy diagram of a recuperated Joule-Brayton PTES cycle (a) charging process. (b) discharging process. The horizontal red and blue lines indicate the temperatures that the hot and cold storage fluids vary between.

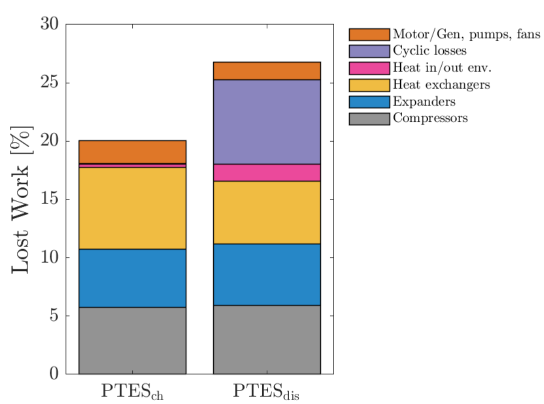

Figure 4: Distribution of exergy losses between different components in charge and discharge

analysis.

A significant quantity of work is lost via ‘cyclic losses’: during charge the hot storage fluid is heated from 300 °C to 565 °C. However, during discharge the hot fluid is cooled down to 325 °C and because it is not returned to its original temperature, this constitutes a loss in efficiency. This occurs because the exit temperature of the discharging expander is relatively hot compared to original hot storage temperature – compare Points 1 and 1’ on the temperature-entropy diagram (Fig. 3). Consequently, the outlet temperature of the recuperator on its high-pressure side (Point 2a’) is hotter than the original hot fluid temperature, which means the hot fluid is not returned to its original temperature. An effective method to reduce the cyclic losses is to increase the discharging pressure ratio which decreases the discharging expander exit temperature.

The energy density of this system is 15 $\mathrm{kWh_e/m^3}$ which is comparable to other TMES systems, such as LAES [8]. This value is a bit lower than Joule-Brayton PTES with packed beds (50 $\mathrm{kWh_e/m^3}$ [17]) but the energy density could be increased by using two stratified tanks rather than four. Compared to other storage systems, PTES has a higher energy density than PHES (0.5-2 $\mathrm{kWh_e/m^3}$) and CAES (3-15 $\mathrm{kWh_e/m^3}$), but a much lower value than lithium-ion batteries ($\approx$300 $\mathrm{kWh_e/m^3}$) [8].

For this nominal design, the total specific capital costs are $C_{\mathrm{pow}} = 2600 \pm 700$ \$/kWh$_\mathrm{e}$ and $C_{\mathrm{en}} = 260 \pm 70$ \$/kWh$_\mathrm{e}$ which are comparable with other thermo-mechanical storage systems, such as CAES and LAES [8]. The extent of the economic uncertainty is illustrated in Fig. 5a. This box-and-whisker diagram shows the range of costs calculated for each component, with median values indicated by a red line. Compressors, expanders and heat exchangers are the main contributors to the capital cost, and these components have considerable uncertainty.

The LCOS is 0.13 $\pm$ 0.03 \$/kWh$_\mathrm{e}$, and the contribution of the capital cost, operations and maintenance cost, and electricity cost to the LCOS is shown in Fig. 5b. Over the lifetime of the plant, the electricity cost makes the largest contribution to the LCOS. In this example, electricity was bought for prices between 0.025–0.075 \$/kWh$_\mathrm{e}$. The lower bound is based on anticipated values for future, unsubsidized, utility-scale wind and solar installations [45]. In some markets, negative electricity prices occur when large quantities of energy are curtailed. The electricity price used here reflects the average value when charging the system every day over the course of a year. It should be noted that in some analyses, the electricity term of the LCOS calculation (Eq. 8) is written as $(E_{\mathrm{in}} - E_{\mathrm{out}})P_{\mathrm{el}} = (1/\eta_{RT} - 1)E_{\mathrm{out}}P_{\mathrm{el}}$ [45] – i.e., it is assumed that the discharged electricity is sold for at least the same price it was bought for, and thus the contribution to the LCOS only represents the electricity that is bought and lost through inefficiencies. Accounting for electricity prices this way, and assuming low electricity costs, substantially reduces the LCOS.

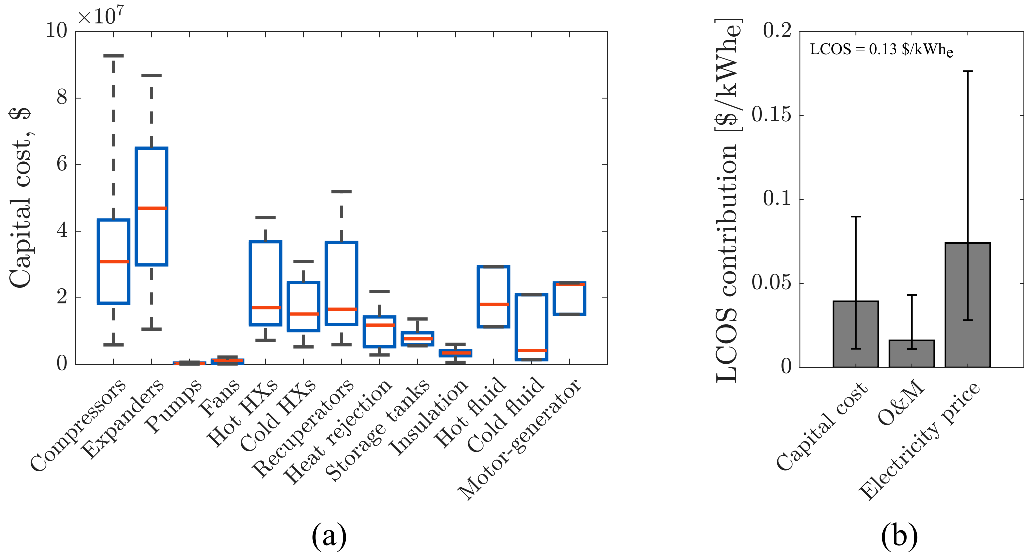

Figure 5: (a) Box-and-whisker plot indicating the distribution of costs expected for each component. Red line indicate the median cost, the box indicates the interquartile range, and the 'whiskers' correspond to the 1% and 99% percentiles. (b) Distribution of the LCOS between capital cost, operations and maintenance costs, and electricity costs for the nominal design. Error bars indicate the mean plus or minus one standard deviation.

Table 3: Upper and lower limits that economic parameters were varied by to assess their influence on the LCOS, see Fig. 6. The O&M is given as a percentage of the capital cost.

	C_{cap}, M$	FCR	O&M, %	P_{el}, $/kWh$_e$	N_{cyc}
Lower bound	190	0.05	1	0.025	250
Upper bound	340	0.10	5	0.060	365

As a further example of the sensitivity of the LCOS to various economic assumptions, several key economic parameters are varied and results are shown in Fig. 6. The capital cost is varied between the mean value of the nominal design plus and minus one standard deviation, and the range of variation of other parameters such as the FCR, O&M, electricity price, and number of cycles per year is given in Table 3. The LCOS has been normalized by the value achieved when each of the parameters is at its mean value to more clearly illustrate the influence of each economic parameter. Each parameter has a roughly $\pm 10 - 20\%$ impact on the LCOS, with the electricity price and capital cost having the largest influence. The FCR is also significant and

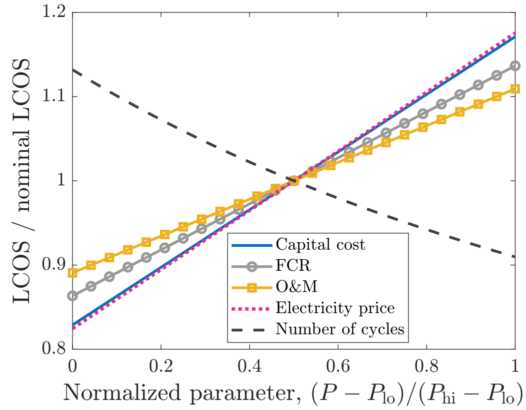

Figure 6: Influence of various economic parameters on the LCOS of the nominal PTES design. Parameters are varied between the minimum and maximum values shown in Table 3. The LCOS has been normalized by the nominal value in Table 2.

combines factors such as the lifetime, discount rate, debt, and taxes. The system lifetime is a significant component of the FCR, with long lifetimes leading to a lower FCR and lower LCOS. The number of cycles per year affects the total energy that is returned to the grid, and more cycles reduce the LCOS. Throughout this article, it is assumed that the system charges and discharges every day (365 cycles per year), although the actual load cycles will depend on the market requirements. This reveals another limitation of the LCOS metric since in some scenarios, electricity storage may cycle very infrequently but earn value by providing firm capacity and dispatchability.

These nominal results indicate that PTES can achieve a respectable round-trip efficiency and LCOS. Further performance improvement can be obtained by system optimization, as discussed in Section 6. First, the influence of each design parameter on the performance is investigated.

5. Discussion: Influence of design parameters

The sensitivity of the round-trip efficiency and the LCOS to several design variables is now considered. Each parameter is varied while the other parameters are kept constant at the nominal values provided in Table 2.

5.1. Heat exchanger design

The heat exchanger design has a significant influence on the performance of this PTES system, since heat exchangers are required to transfer energy into and out of the storage, and also within the cycle itself. The heat exchanger is characterized by the effectiveness, ε and fractional pressure loss, f_p as defined in Section 3.1. All heat exchangers are assumed to have the same ε and f_p, with the exception of the air-cooled heat exchangers, which have fixed values of $\varepsilon = 0.9$ and $f_p = 0.1\%$.

As expected, the round-trip efficiency increases monotonically with effectiveness and decreases with fractional pressure loss, as shown in Fig. 7a. For a typical effectiveness of 85% the round-trip efficiency is only 40% and the majority of exergy losses occurs within the heat exchangers. Increasing the effectiveness reduces the heat exchanger exergy losses, and achieving a round-trip efficiency greater than 55% requires $\varepsilon > 95\%$ and very low pressure losses. Such heat exchangers require very large heat exchange areas, and may present engineering challenges. Large heat exchange areas increase capital costs but Fig. 7b indicates that the increased efficiency is worth the higher cost up to $\varepsilon = 0.95$, at which point a minimum LCOS occurs. Increasing the effectiveness further leads to a sharp increase in LCOS as the limit of infinite heat exchanger area is approached at $\varepsilon = 1$. The value of ε that minimizes the LCOS will depend on project finances and projected lifetimes.

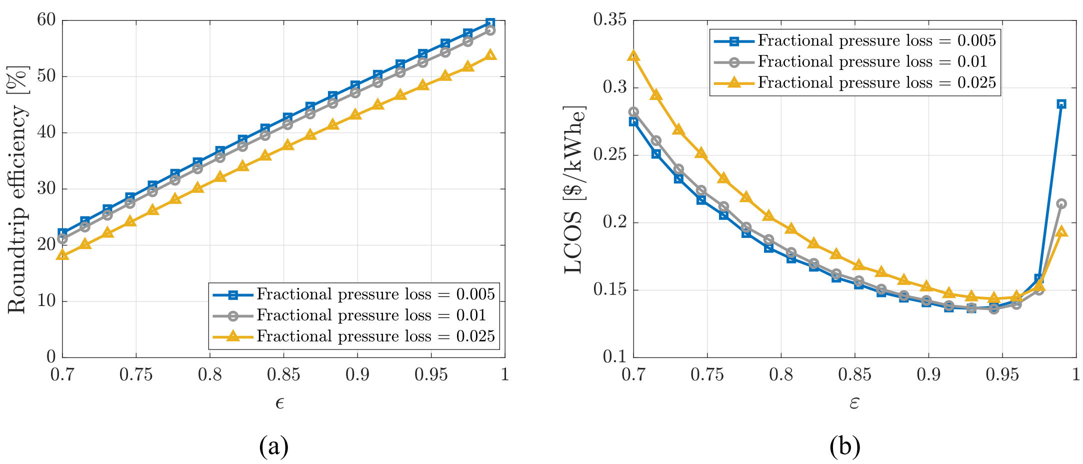

Figure 7: Effect of heat exchanger effectiveness and pressure losses on (a) Round-trip efficiency and (b) Levelized cost of storage.

5.2. Discharging pressure ratio

The discharging pressure ratio, β_{dis} influences the cyclic losses as discussed in Section 4. The discharging expander inlet temperature (Point 2' on Fig. 3b) is effectively fixed by the hot storage temperature, so increasing the discharging pressure ratio reduces the expander outlet temperature (Point 1'). In turn, this reduces the

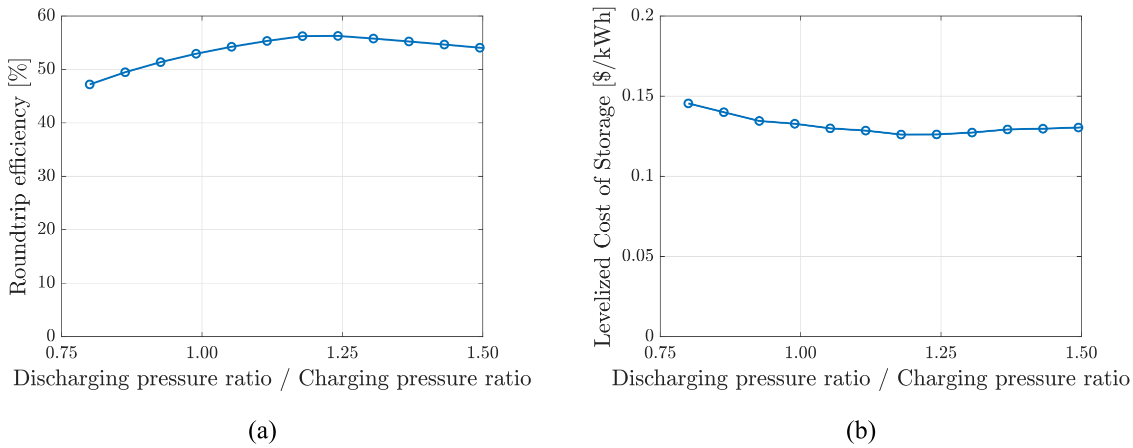

Figure 8: Effect of discharging pressure ratio on (a) Round-trip efficiency and (b) Levelized cost of storage.

inlet temperature to the hot side of the recuperator (1'), and thus reduces the exit temperature of the recuperator's cold side (3'). Consequently, the discharging pressure ratio affects the temperature that the hot storage fluid is returned to at the end of discharge.

As noted in Section 4, when β_{dis} equals the charging pressure ratio, β_{chg} the expander exit temperature is relatively hot and at the end of discharge the hot fluid is hotter than its temperature at the start of charge. This requires energy to be rejected to ensure a cyclic process and thus represents a loss in efficiency. Increasing the discharging pressure ratio therefore leads to an improvement in efficiency and LCOS, as demonstrated in Fig. 8. An optimal value is obtained when the hot storage fluid is returned exactly to its starting temperature. If the discharging pressure ratio is increased further, then there is the risk that the hot fluid would be cooled to temperatures below the original value, in which case extra heat would have to be added to the cycle to avoid over-discharge.

5.3. Choice of hot storage liquid

The choice of hot storage fluid has a profound impact on the design and performance of the PTES cycle. Liquid storage fluids typically have limited operating temperature ranges. The upper temperature limit may be constrained by thermal decomposition or phase change; and this temperature has a significant influence on the round-trip efficiency and energy density, as well as determining which materials are required in the heat exchangers. The lower temperature limit can be constrained by freezing (such as for molten salts) or high pumping costs due to increased viscosity (for thermal oils). This lower temperature also impacts the energy density: the smaller the operating temperature range, the larger the fluid and storage volume and thus the higher the cost. For the recuperated Joule-Brayton cycle, the lower temperature limit also constrains the charging compressor inlet temperature (Point 1 on Fig 3a). For instance, the relatively high freezing point of molten salts suggests that compressor inlet temperatures will be over 250 °C – which is somewhat hotter than the inlet temperatures to conventional compressors, suggesting that Joule-Brayton PTES turbomachinery may require significant technological development.

In this section, four hot storage fluids are considered: mineral oil, synthetic oil, nitrate molten salt, and chloride molten salt. In each case, the cycle is operated at the maximum temperature for each fluid and the compressor inlet temperature was varied (effectively varying the lower temperature of the hot fluid). For each compressor inlet temperature, the discharging pressure ratio is adjusted to reduce the cyclic losses. Further details for the four fluids are provided in Table 4.

Table 4: Thermal properties and cost factors for several hot storage fluids. Thermal properties are the average over the operating temperature range. A range of costs are given based on values from the literature and vendors.

Fluid type	Details	$T_{\min}$ °C	$T_{\max}$ °C	c_p kJ/kg.K	ρ kg/m^3	Cost $/kg
Mineral oil	Shell heat transfer oil S2	10	300	2.37	775	0.5-2.5
Synthetic oil	Diphenyl oxide-biphenyl	10	393	2.06	886	0.5-3.1
Nitrate molten salt	$NaNO_3$-KNO_3	230	565	1.51	1840	0.5-1.3
Chloride molten salt	NaCl-KCl-$MgCl_2$	450	750	1.03	1460	0.4-1.1

Operating at higher temperatures either requires specialized materials or larger volumes of metals to resist creep, leading to higher costs. Here it is assumed that this predominantly affects the heat exchanger costs as storage tanks are internally insulated. Cost factors are applied to the hot heat exchanger and recuperator to reflect the influence of maximum temperature, see Table 1.

Increasing the maximum temperature of the cycle tends to lead to higher round-trip efficiencies, as shown in Fig. 9a. For each material there is an optimal compressor inlet temperature which arises due to a trade-off between exergy losses in the turbomachinery and heat exchangers. Thus, for a given heat exchanger design and maximum temperature, the value of T_1 can be adjusted to minimize the lost work.

The benefits of achieving higher efficiencies by increasing the system temperature must be balanced against higher capital costs due to more expensive heat exchanger materials. As indicated in Fig. 9b, the minimum LCOS of systems with nitrate salts and chloride salts are very similar. In this figure, sharp changes in LCOS can be

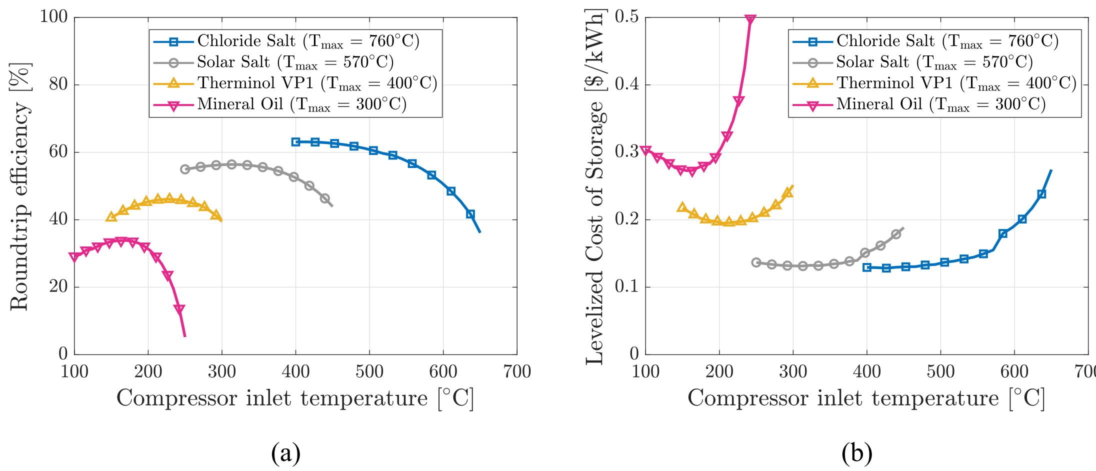

Figure 9: Influence of hot storage fluid and compressor inlet temperature on (a) Round-trip efficiency (b) Levelized cost of storage.

observed close to compressor inlet temperatures of 400 °C and 600 °C, where the recuperator material transitions from carbon steel to stainless steel, and stainless steel to nickel alloy, respectively.

Systems using mineral oils and synthetic fluids avoid the use of expensive metals in the heat exchangers. However, these systems have higher costs for two predominant reasons: firstly, they have small temperature differences across the cycle leading to low energy densities and high storage costs for a given energy output; secondly, they have lower efficiencies which requires larger work inputs during charge and therefore larger turbomachinery. The costs of these systems could be reduced by removing the recuperator which would reduce heat exchanger costs. However, the low efficiencies and power densities would still lead to higher costs than PTES systems with molten salts.

5.4. Duration of charge compared to discharge

So far it has been assumed that the charging and discharging durations are equal. This means that the charging power input exceeds the discharging power output – for example, for the nominal design in Table 2, $\dot{W}_{\mathrm{dis}} = 100$ MW$_{\mathrm{e}}$, whereas the charging work input is $\dot{W}_{\mathrm{chg}} = \dot{W}_{\mathrm{dis}}/\eta_{RT} = 188$ MW$_{\mathrm{e}}$. In this section, the charging duration τ_{chg} is varied while keeping the discharging duration, τ_{dis} and power output constant.

The round-trip efficiency increases if τ_{chg} is increased *or* decreased by a small amount as shown in Fig. 10a. This is predominantly the result of reduced entropy generation in the heat exchangers, and to a lesser extent, the behaviour of the motor-generator. The geometry of the heat exchangers is designed to meet the performance requirements (effectiveness and pressure loss) during the period with highest mass flow rate. When the charging and discharging durations are equal, the mass flow rates through the heat exchangers are approximately the same during charge and discharge. If $\tau_{\text{chg}} > \tau_{\text{dis}}$, then the charging mass flow rate is reduced compared to the discharging mass flow rate. As a result, the heat transfer performance (e.g. the number of heat transfer units, NTU) improves and the pressure losses reduce. Eventually, a maximum round-trip efficiency is reached before further changes to the charging duration lead to a reduction in performance. This is due to reduced flow rates in the recuperator and a transition from turbulent to laminar flow which reduces the heat transfer performance, and therefore increases exergy losses, see Fig. 11. Similarly, if $\tau_{\text{chg}} < \tau_{\text{dis}}$, the heat exchangers are designed for the larger mass flow rate, which occurs during charge, and the heat exchanger performance is improved during discharge, leading to a higher round-trip efficiency.

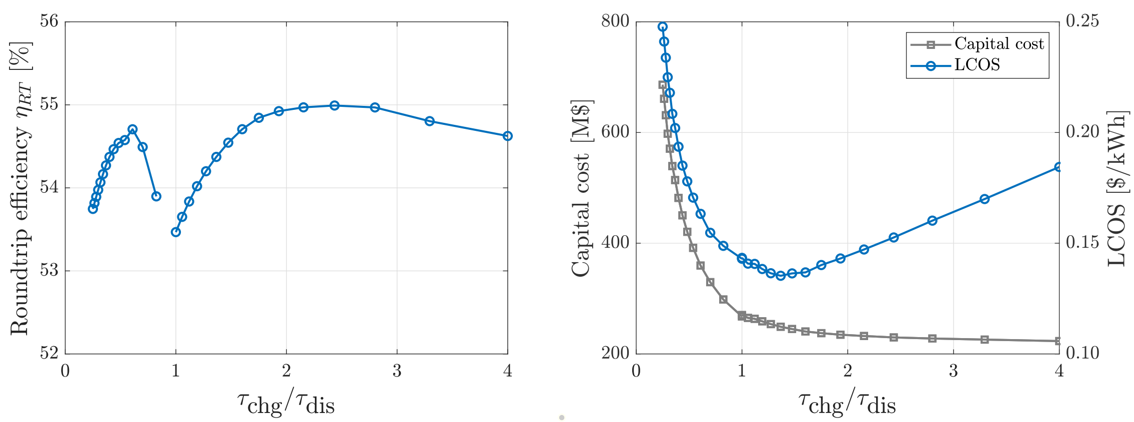

(a) (b)

Figure 10: Effect of charge duration compared to discharge duration on round-trip efficiency. (a) Round-trip efficiency. (b) Capital cost and Levelized cost of storage.

The capital cost is also affected by the duration of charge and discharge. When $\tau_{\text{chg}} > \tau_{\text{dis}}$ the capital cost reduces (Fig. 10b): the reduced charging power input means that smaller compression and expansion machinery is required, as well as a smaller motor. The improved efficiencies and reduced costs of using longer charging durations leads to a lower LCOS as shown in Fig. 10b. However, the LCOS only decreases up to $\tau_{\text{chg}}/\tau_{\text{dis}} = 1.4$ at which point it begins to increase again. In this case, the discharging duration is fixed at 10 hours, and when $\tau_{\text{chg}} > 14$h the total cycle duration exceeds 24 hours. This reduces the number of full charge-discharge cycles

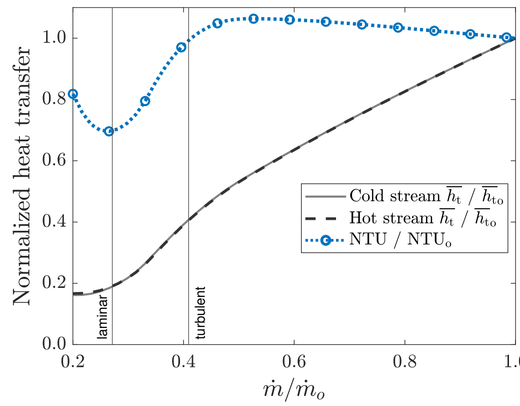

Figure 11: Variation in average heat transfer coefficient and number of heat transfer units (NTU) with mass flow rate in the recuperator. All variables have been normalized by their value at the design point, which in this case corresponds to a mass flow rate of 100 kg/s.

per year and therefore reduces the total energy delivered by the storage. It should be noted that systems that cycle a different number of times per year are likely to provide different functions and cannot be easily compared to one another.

6. Optimization of pumped thermal energy storage and comparison with lithium-ion batteries

6.1. Multi-objective optimization

The trade-off between cost and efficiency is investigated using multi-objective optimization algorithms. These methods find Pareto fronts which are surfaces that show the spread of optimal designs. Most engineering systems exhibit a trade-off between cost and efficiency. A Pareto front will capture the most efficient and expensive solutions on one end of the surface, and the cheapest and least efficient solutions at the other end. Intermediate points reveal the compromise between the two objectives (in practice, multiple objectives may be used). This approach is useful not just for evaluating the optimum performance and optimal designs, but also identifying which design parameters influence a design's position on the trade-off surface.

Stochastic algorithms have previously been applied to PTES systems [17] and are an appropriate method, as multiple objectives are evaluated for numerous design variables with a numerical algorithm. In this study, a multi-objective particle swarm optimization (MOPSO) was found to give reasonable performance. MOPSO uses a 'swarm' of particles that share information and 'flock' towards optimal locations [46].

The PTES multi-objective optimization problem has two objectives; to maximize round-trip efficiency and minimize the levelized cost of storage. The optimization problem is arranged as a minimization problem, such that the objectives are expressed as:

$$f_1 = 1 - \eta_{RT} \tag{9}$$

$$f_2 = \mathrm{LCOS} \tag{10}$$

The design variables are the heat exchanger effectiveness, the heat exchanger pressure loss factor, the compressor inlet temperature T_1, and the discharging pressure ratio β_{dis}. Upper and lower limits of each of the design variables are given in Table 5.

The choice of hot storage fluid and maximum temperature, T_2 is investigated with separate optimization studies. The results of Section 5.3 suggested that nitrate and chloride molten salts outperformed fluids such as mineral oil and synthetic oil. However, it was unclear whether the higher efficiencies justified the increased cost of high-temperature systems. Nitrate molten salts have maximum operating temperatures of 565 °C, but recent research has suggested that thermal stability may be maintained up to 600 °C by carefully managing the gas composition in the tanks [47]. Chloride molten salts can be operated up to 750 °C, although lower temperatures may reduce corrosion and engineering challenges.

Table 5: Upper and lower limits of the design variables used in multi-objective optimization studies.

Design variable		Minimum	Maximum
ε		0.7	0.99
f_p		0.005	0.05
β_{dis}		0.8	1.5
T_1 (nitrate salt)	°C	250	450
T_1 (chloride salt)	°C	450	600

Pareto fronts for four cases – nitrate salts with maximum temperatures fixed at T_2 = 560 °C and 600 °C, and chloride salts at T_2 = 650 °C and 750 °C – are shown in Fig. 12a. The Pareto fronts do not cross at any point. Therefore, for a given cost, the most efficient system always uses chloride salts at 750 °C. Similarly, for a given round-trip efficiency, chloride salts at 750 °C are the most cost-effective solution. Likewise, it is always preferable to use nitrate salts at 600 °C rather than 565 °C, if possible. The least suitable solution has chloride salts at 650 °C since this system has expensive heat exchangers, but has not maximized the efficiency that those exchangers can provide. This suggests that chloride salt systems should only be implemented if they can be operated at their maximum temperature.

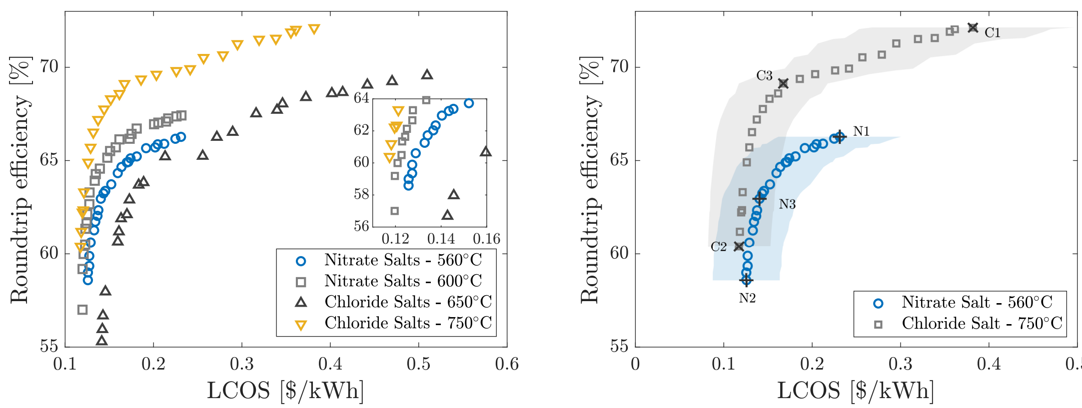

(a) (b)

Figure 12: Pareto fronts illustrating the trade-off between round-trip efficiency and LCOS (a) Pareto frints for nitrate and chloride salts and different maximum temperatures (b) Pareto fronts for nitrate and chloride salts. The shaded band indicates the LCOS plus and minus one standard deviation.

Table 6: Design variables and results for select cases along the Pareto fronts, see Fig. 12b.

Case:		N1	N2	N3	C1	C2	C3
ε		0.99	0.96	0.98	0.99	0.95	0.98
f_p		0.005	0.006	0.007	0.005	0.020	0.010
β_{dis}		1.19	1.18	1.23	1.25	1.24	1.26
T_1	°C	370	322	326	474	455	457
η_{RT}	%	66	59	63	72	60	69
LCOS	$/kWh$_\text{e}$	0.23	0.13	0.14	0.38	0.12	0.17

The inset figure in Fig. 12a indicates that each system has similar minimum values of LCOS. The LCOS plus or minus one standard deviation is illustrated in Fig. 12b for two cases. The economic uncertainty is reasonably large, and it is unclear whether chloride salt PTES systems are definitely preferable to nitrate salt PTES systems. A detailed engineering cost appraisal is necessary to reduce the uncertainty in these estimates.

The design variables are expected to change along the length of the Pareto front, as certain values will reduce costs and other values will increase efficiencies. Design

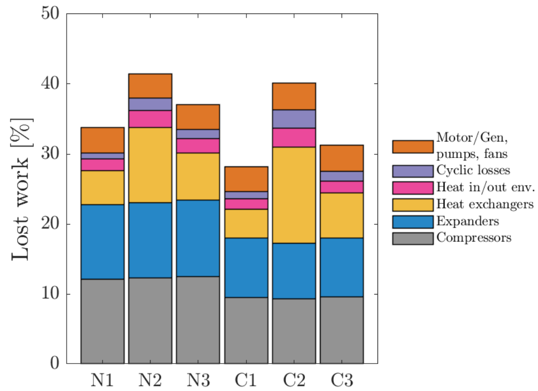

Figure 13: Distribution of exergy losses between different components for select cases along the Pareto fronts, corresponding to Fig. 12b.

variables for select cases are presented in Table 6. These cases are illustrated on Fig. 12b, and correspond to (1) maximizing η_{RT} (2) minimizing LCOS (3) finding a compromise between the two objectives by choosing a point close to the 'knee' of the Pareto front. Further insight is gained by considering the various sources of exergy loss as shown in Fig. 13. Heat exchanger design (ε and f_p) varies most significantly along the Pareto front. The effectiveness saturates at its upper constraint to maximize η_{RT} by minimizing heat exchanger losses, while values that minimize the LCOS are closer to 0.95, which is similar to the results shown in Fig. 7b. The compressor inlet temperature T_1 is higher when maximizing η_{RT}. However, this reduces the temperature difference between the two hot tanks, which requires larger storage volumes for a given storage duration. Therefore, designs which minimize the LCOS have lower values of T_1. Fig. 13 indicates that only the heat exchanger exergy losses vary substantially along the Pareto front, whereas losses in other components are fairly constant. Thus, when designing these PTES systems, heat exchangers should be considered first and the remaining system can be optimized around them.

6.2. Cost comparison with lithium-ion batteries

The techno-economic models and results presented here are most suitable for comparing different PTES designs and configurations. However, it is instructive to provide some context by comparing the optimal results of Section 6.1 with cost estimates for other storage technologies. Lithium-ion batteries (LiB) have rapidly reduced in cost in recent years as a result of increasing deployment in electric vehicles and utility-scale projects, and these cost reductions are expected to continue [48].

LiB costs were obtained from data in Lazard's LCOS Analysis [49] which provides upper and lower estimates, and these values are comparable with those obtained using the learning curves proposed in Ref. [48] and the range of values predicted in Ref. [50]. Costs may be separated into power costs $\bar{c}_{\text{pow}}$ and energy costs $\bar{c}_{\text{en}}$, such that the total capital cost is given by $C_{\text{cap}} = (\bar{c}_{\text{pow}} + \bar{c}_{\text{en}}\tau_{\text{dis}})\dot{W}_{\text{dis}}$. The LiB costs used here are $\bar{c}_{\text{pow}}$ = 51-75 \$/kW$_{\text{e}}$ and $\bar{c}_{\text{en}}$ = 164-300 \$/kWh$_{\text{e}}$.

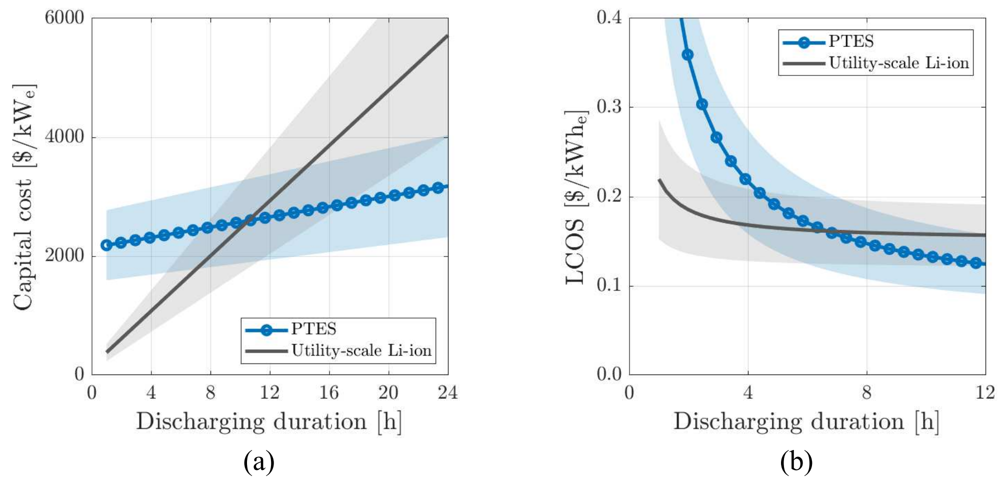

Figure 14: Costs of a 100 MW$_{\text{e}}$ storage system for various discharging durations. Costs for PTES show the mean value of optimal design N2 (Table 6) plus and minus the standard deviation. Utility-scale Li-ion costs are also shown with the shaded region indicating the range of values proposed in Ref. [49]. (a) Total capital cost per unit power. (b) LCOS.

The costs of LiB and PTES are compared in Fig. 14 for a range of discharging durations. PTES costs correspond to the optimal design N2 in Table 6, and the blue band indicates the standard deviation of the results. PTES has a relatively high power cost (which includes heat exchangers, turbomachinery, and motor-generator) with $\bar{c}_{\text{pow}} = 2140 \pm 540$ \$/kW$_{\text{e}}$, and is therefore more expensive than LiB for short-duration storage. However, the marginal cost of the storage components is very low ($\bar{c}_{\text{en}} = 43 \pm 11$ \$/kWh$_{\text{e}}$), such that the total capital cost does not increase substantially as the storage duration is increased. The analysis indicates that PTES is competitive with conservative LiB cost predictions at discharging durations of 6-8 h, and with more aggressive LiB cost targets at >12 h.

The capital cost only reflects the initial investment, whereas the LCOS also includes factors such as the lifetime, efficiency, and O&M costs. LiB have shorter lifetimes (15 years) than PTES which results in a higher FCR, which is approximately 0.11, compared to 0.07 for PTES. It is assumed that batteries are operated

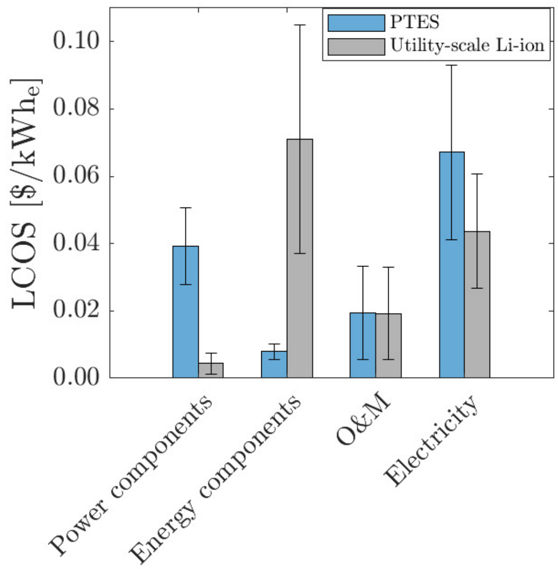

Figure 15: Contribution of economic factors to the LCOS for PTES and LiB for 100 MW_e systems with 10 hours of discharging. PTES results correspond to optimal design N2 in Table 6. Error bars indicate the mean plus/minus one standard deviation for PTES or the range suggested in Ref. [49] for LiB

.

to a maximum depth of discharge of 80%, which corresponds to over-sizing the battery by 25% for a given power output. (Similarly, PTES tanks are oversized by 10%). LiB have a round-trip efficiency of 90% as compared to 59% for the N2 PTES design. Including lifetime costs leads to PTES systems being competitive over a larger range of discharging durations than the capital cost would suggest: PTES systems have a similar LCOS to conservative and agressive LiB cost estimates at discharging durations of 4-6h and 8-12h, respectively. PTES can be made competitive over a larger range of discharging durations by reducing $\bar{c}_{\mathrm{pow}}$ – i.e., reducing heat exchanger and turbomachinery costs.

The contribution of different costs to the LCOS are shown in Fig. 15 for systems which discharge for 10 h. The most significant contributions to the PTES LCOS come from high costs of power components and a large expenditure on electricity for charging. LiBs have lower electricity costs due to the higher round-trip efficiency. The LiB LCOS is dominated by the high value of $\bar{c}_{\mathrm{en}}$ which ultimately leads to higher LCOS values than PTES. It should be noted that this analysis assumes both systems charge and discharge once per day. However, it is likely that real load cycles will be different to this, and that PTES and LiB load cyles may not be the same due to their different efficiencies and operational characteristics.

7. Conclusions

In this article, a techno-economic model of Pumped Thermal Energy Storage (PTES) systems based on a recuperated Joule-Brayton cycle and using two-tank liquid storage is developed. The performance and cost of this system is strongly dependent on the heat exchanger design. The technical model calculates the heat exchanger geometry which, therefore, enables an accurate assessment of the performance and capital cost of the system. The results indicate that the use of heat exchangers with very high effectiveness values up to 0.95 can be justified economically due to significant performance improvements they offer to the system. However, increasing the effectiveness further leads to rapidly increasing costs. Further analysis is required to clarify the manufacturing challenges associated with high-effectiveness heat exchangers.

The choice of the hot storage liquid places constraints on the operating temperatures of the system. Several hot storage liquid media are considered. Nitrate molten salts can be operated up to 565 °C, whereas novel chloride salts may be operated up to 750 °C. Increasing the maximum temperature leads to larger round-trip efficiencies, but the increased temperatures require more expensive materials in some of the heat exchangers. Therefore, the LCOS of systems using nitrate salt and chloride salt as liquid storage media are similar.

A multi-objective optimization algorithm is used to evaluate the trade-off between LCOS and round-trip efficiency, as well as investigate the most suitable hot storage fluid. PTES with chloride salts was found to have lower values of LCOS and higher efficiencies than systems using nitrate molten salts. For example, the most cost-effective chloride salt system costs 0.12 ± 0.03 \$/kWh$_e$ and has a round-trip efficiency of 60%, whereas the most cost-effective nitrate salt system achieves values of 0.13 ± 0.03 \$/kWh$_e$ and 59%, respectively. The uncertainty in the cost estimates is rather large, and further analysis should improve the economic accuracy.

Compared to utility-scale lithium-ion batteries (LiB), PTES has high power component costs but low energy storage component costs. This means that additional storage can be added without significantly increasing total capital costs. Furthermore, PTES has longer lifetimes than LiB, and as a result, PTES can achieve lower lifetime costs (LCOS) than LiBs at discharging durations greater than 6 h. By further reducing the capital cost of PTES systems through key power component selection and development, such as the heat exchangers and turbomachinery, PTES can be competitive over a larger range of energy storage applications, including applications that benefit from integration with external thermal sources and sinks (e.g., solar or waste), by utilizing and/or providing thermal energy along with electrical energy during operation.

Acknowledgements

This work was authored in part by the National Renewable Energy Laboratory, operated by Alliance for Sustainable Energy, LLC, for the U.S. Department of Energy (DOE) under Contract No. DE-AC36-08GO28308. Funding was provided by U.S. Department of Energy Office of Energy Efficiency and Renewable Energy Solar Energy Technologies Office. The views expressed in the article do not necessarily represent the views of the DOE or the U.S. Government. The U.S. Government retains and the publisher, by accepting the article for publication, acknowledges that the U.S. Government retains a nonexclusive, paid-up, irrevocable, worldwide license to publish or reproduce the published form of this work, or allow others to do so, for U.S. Government purposes. This work was also supported by the UK Engineering and Physical Sciences Research Council (EPSRC) [grant numbers EP/S032622/1 and EP/R045518/1]. PF-A was partially supported by the UK EPSRC [grant numbers EP/P021867/1 and EP/P004709/1]. The authors gratefully acknowledge Mark Mehos, Craig Turchi, and Matthew Bauer for valuable discussions.

Appendix A. Heat exchanger algorithms

Appendix A.1. Sizing procedure

The sizing procedure determines a set of heat exchanger geometrical parameters that satisfy the specified effectiveness ε and pressure loss f_p for a given set of inlet conditions (i.e., the inlet values of $\dot{m}$, h and p for the two fluids). Apart from the previous inputs, the sizing procedure also requires the hydraulic diameter D to be specified, which depends strongly on the heat exchanger technology. The present work is limited to circular-tube heat exchangers, which have hydraulic diameters typically ranging from a few mm up to several cm [51], and a value of $D = 5$ mm is used in here. In general, small tubes are preferred because they lead to more compact devices [52], which is due to higher heat transfer coefficients and higher surface-to-volume ratios [34]. The sizing procedure assumes that the hydraulic diameters and flow areas of the two sides of the heat exchanger are the same, i.e. $D_1 = D_2 \equiv D$ and $A_{\mathrm{f1}} = A_{\mathrm{f2}} \equiv A_{\mathrm{f}}$. This may, in some cases, result in slightly sub-optimal designs and conservative cost estimates, but is not far from what is encountered in many practical designs and is justified by the significant gain in speed and simplicity of the algorithm.

The sizing procedure is summarized in Fig. A.16a and follows the steps below.

(i) The heat transfer rate, $\dot{Q}$, is computed according to ε and the set of inlet conditions.

(ii) The heat exchanger is divided in sections of equal $\mathrm{d}\dot{Q}$, and a T-$\dot{Q}$ diagram is drawn. This is used to obtain information on the variation of fluid thermophysical properties along the length of the heat exchanger.

(iii) An iterative process is performed over values of flow area, A_f, until the pressure losses meet the objective value, according to the following the steps.

(iv) For each value of A_f, the mass flux, G, the Reynolds and Prandtl numbers, Re and Pr, the convective heat transfer coefficient, h_t, and the friction coefficient, c_f, are all computed at each heat exchanger section. Standard correlations for fully developed internal flow in circular tubes (e.g. see [53]) are employed and are summarized in Table A.7. The heat transfer coefficient is computed via the Nusselt number in the usual way, $h_\mathrm{t} = \mathrm{Nu}\, k/D$. The flow is treated as laminar for Re $\leq$ 2000 and as turbulent for Re $\geq$ 3000. In between, the values for transition flow are obtained by interpolation.

(v) The overall heat transfer coefficient, U, is computed at each section, and it is used together with the ΔT-$\dot{Q}$ distribution to compute the required heat transfer area, A, and the required heat exchanger length, L, according to the equations,

$$U = \frac{1}{\dfrac{1}{h_\mathrm{t1}} + \dfrac{1}{h_\mathrm{t2}}} \tag{A.1}$$

$$A = \int \frac{d\dot{Q}}{U\,\Delta T} \tag{A.2}$$

$$L = \frac{D A}{4 A_\mathrm{f}} \tag{A.3}$$

where it is implicit that the heat transfer area and length of the two streams is the same, which is a consequence of the streams having the same flow area and hydraulic diameter, as discussed above.

(vi) Pressure losses are obtained from c_f and integrated over the heat exchanger length. For the first stream,

$$f_{p1} = \int \frac{-2\, c_\mathrm{f1}\, G_1^2\, \mathrm{d}L}{D\, \rho_1\, p_1} \tag{A.4}$$

and similarly for the second stream.

(vii) The predicted pressure losses at each side, f_{p1} and f_{p2}, are compared to the objective pressure loss, f_p.

(viii) The value of A_f is changed and the previous steps are repeated until $\max(f_{p1}, f_{p2}) = f_p$, ensuring that none of the channels exceeds the objective pressure loss. Since f_{p1} and f_{p2} are monotonic functions of A_f, the converging value of A_f is efficiently found with a bisection algorithm that is readily available in Matlab.

Table A.7: Friction coefficient and Nusselt number for fully developed internal flow [53].

Regime	c_f	Nu
Laminar	16/Re	4.36
Turbulent	$\dfrac{1}{(1.58\ln(\mathrm{Re}) - 3.28)^2}$	$\dfrac{(c_\mathrm{f}/2)(\mathrm{Re}-1000)\,\mathrm{Pr}}{1 + 12.7\,(c_\mathrm{f}/2)^{1/2}\left(\mathrm{Pr}^{2/3}-1\right)}$

Appendix A.2. Off-design model

Once the geometry of the heat exchanger is known, it can be used to predict outlet conditions for any given set of inlet conditions. The off-design model used to achieve this is summarized in Fig. A.16b. As shown in the flow chart, the off-design model follows similar steps to the sizing procedure, the main difference being that, rather than iterating over A_f until the pressure losses converge, the off-design model iterates over $\dot{Q}$ until the heat transfer balance in Eq. A.2 converges. The equations and correlations employed are the same as those described in Appendix A.1.

Appendix A.3. Validation

The heat exchanger sizing procedure and the heat exchanger off-design model were validated against data from Figley et al., who describe a CFD simulation of a high-temperature helium recuperator [54]. The recuperator in question is a counterflow heat exchanger which satisfies the main geometrical assumptions described in Appendix A.1: straight channels, equal hydraulic diameter for both streams, and equal cross-sectional area (i.e., flow area) for both streams. However, the device is a printed-circuit heat exchanger (PCHE) that features semi-circular rather than circular channels. While the heat transfer and flow friction characteristics for circular and semi-circular channels show only minor differences, these were accounted for during the validation study to ensure a more precise comparison. Correlations for semi-circular channels are described in [54].

Table A.8: Design point specifications for validation of sizing procedure.

Parameter	Unit	Value
$\dot{m}_{\mathrm{h}}$, $\dot{m}_{\mathrm{c}}$	kg/s	0.0056
$p_{\mathrm{h,in}}$, $p_{\mathrm{c,in}}$	bar	30
$T_{\mathrm{h,in}}$	K	1173
$T_{\mathrm{c,in}}$	K	813
D_{h}, D_{c}	mm	1.222
ε	%	76.1
$f_{p,\mathrm{h}}$	%	0.175

Table A.9: Geometrical parameters computed by the sizing procedure compared to the original specifications by Figley et al. [54]. The values of L, A_{f} and A are the same for the hot and the cold streams.

Parameter	Unit	Original	Predicted	Diff. [%]
L	mm	247.2	237.3	4.0
A_{f}	mm^2	188.5	190.3	0.9
A	m^2	0.152	0.148	3.0

Table A.8 shows the reference design point specifications used as inputs of the sizing procedure, including inlet conditions and performance objectives, while table A.9 shows the output geometrical parameters. It can be seen that the geometry predicted by the sizing procedure is very similar to the original specifications by Figley et al., showing a maximum disagreement of 4%.

The predicted geometry was then used to run a number of off-design simulations under the conditions described by Figley et al., the results of which are shown in Fig. A.17. The plots display a good agreement between the 1D off-design model and the CFD model by Figley et al., with differences being generally below ±5%.

References

[1] Renewable Energy Policy Network for the 21st Century, Renewables 2020 Global Status Report, REN21, 2020.
URL `http://www.ren21.net/resources/publications/`

[2] Lazard, Lazard's Levelized Cost of Energy Analysis - Version 14.0, Tech. rep., Lazard (2020).
URL `https://www.lazard.com/perspective/levelized-cost-of-energy-and-levelized-cost-of-storage-2020/`

[3] J. P. Palutikof, H. F. Cook, T. D. Davies, Effects of geographical dispersion on wind turbine performance in England: A simulation, Atmospheric Environment Part A, General Topics 24 (1) (1990) 213–227. doi:10.1016/0960-1686(90)90458-Y.

[4] D. J. C. Mackay, Sustainable Energy — without the hot air, UIT Cambridge Ltd., 2009. doi:10.1109/PES.2004.1373296.
URL `www.withouthotair.com`

[5] M. Park, J. Ryu, W. Wang, J. Cho, Material design and engineering of next-generation flow-battery technologies, Nature Reviews Materials 2 (1). doi:10.1038/natrevmats.2016.80.

[6] S. Georgiou, M. Aunedi, G. Strbac, C. N. Markides, On the Value of Liquid-Air and Pumped-Thermal Electricity Storage systems in low-carbon electricity systems, Energy 193. doi:10.1016/j.energy.2019.116680.

[7] P. Tixador, Superconducting magnetic energy storage: Status and perspective, in: IEEE/CSC & ESAS EUROPEAN SUPERCONDUCTIVITY NEWS FORUM, 2008, pp. 1–14.

[8] A. Olympios, J. McTigue, P. Farres-Antunez, A. Romagnoli, W. Steinmann, A. Thess, L. Wang, H. Chen, Y. Li, Y. Ding, C. N. Markides, Progress and prospects of thermo-mechanical energy storage – a critical review, IOP Progress in Energy 3. doi:10.1088/2516-1083/abdbba.

[9] O. Walter, A. Tremel, M. Prenzel, S. Becker, J. Schaefer, Techno-economic analysis of hybrid energy storage concepts via flowsheet simulations, cost modeling and energy system design, Energy Conversion and Management 218 (2020) 112955. doi:10.1016/j.enconman.2020.112955.

[10] W.-D. Steinmann, D. Bauer, H. Jockenhöfer, M. Johnson, Pumped thermal energy storage (PTES) as smart sector-coupling technology for heat and electricity, Energy 183 (2019) 185–190. doi:10.1016/j.energy.2019.06.058.

[11] P. Denholm, W. Cole, A. W. Frazier, K. Podkaminer, N. Blair, The Four Phases of Storage Deployment: A Framework for the Expanding Role of Storage in the U.S. Power System, NREL Technical Report NREL/TP-6A20-77480.

[12] F. Marguerre, Ueber ein neues verfahren zur aufspeicherung elektrischer energie, Mitteilungen der Vereinigung der Elektrizitatswerke 354 (1924) 27–35.

[13] B. Weissenbach, Thermal energy storage device, patent No. EP/0003980 A1 (1979).

[14] T. Desrues, J. Ruer, P. Marty, J. Fourmigué, A thermal energy storage process for large scale electric applications, Applied Thermal Engineering 30 (5) (2010) 425–432. doi:10.1016/j.applthermaleng.2009.10.002.

[15] J. MacNaghten, J. S. Howes, Energy storage, international Patent No. WO 2009/044139 A2 (2009).

[16] A. White, G. Parks, C. N. Markides, Thermodynamic analysis of pumped thermal electricity storage, Applied Thermal Engineering 53 (2) (2013) 291–298. doi:10.1016/j.applthermaleng.2012.03.030.

[17] J. D. McTigue, A. J. White, C. N. Markides, Parametric studies and optimisation of pumped thermal electricity storage, Applied Energy 137 (2015) 800–811. doi:10.1016/j.apenergy.2014.08.039.

[18] A. White, J. McTigue, C. Markides, Analysis and optimisation of packed-bed thermal reservoirs for electricity storage applications, Proceedings of the Institution of Mechanical Engineers, Part A: Journal of Power and Energy 230 (7). doi:10.1177/0957650916668447.

[19] J. D. McTigue, C. N. Markides, A. J. White, Performance response of packed-bed thermal storage to cycle duration perturbations, Journal of Energy Storage 19 (August) (2018) 379–392. doi:10.1016/j.est.2018.08.016.

[20] T. Fasquelle, Q. Falcoz, P. Neveu, J. Ho, A temperature threshold evaluation for thermocline energy storage in concentrated solar power plants, Applied Energy 212 (2018) 1153–1164. doi:10.1016/j.apenergy.2017.12.105.

[21] M. Morandin, S. Henchoz, M. Mercangöz, Thermoelectric energy storage: a new type of large scale energy storage based on thermodynamic cycles, World Engineers' Convention.

[22] P. Farres-Antunez, A. J. White, Thermodynamic strategies for pumped thermal exergy storage (PTES) with liquid reservoirs, in: UK Energy Storage Conference, Birmingham, UK, 2016, pp. 1–45. doi:10.17863/CAM.64182.

[23] J. D. McTigue, P. Farres-Antunez, C. N. Markides, A. J. White, Pumped thermal energy storage with liquid storage, in: Encyclopedia of Energy Storage, Elsevier, 2021. doi:doi.org/10.1016/B978-0-12-819723-3.00054-8.

[24] B. R. Bollinger, Malta Pumped Heat Electricity Storage (PHES) for Coal Exit and Energy Transition from Fossil to Renewable Energies, in: 2nd International Workshop on Carnot Batteries, Stuttgart, Germany, 2020, pp. 1–15.

[25] Y. Zhao, M. Liu, J. Song, C. Wang, J. Yan, C. N. Markides, Advanced exergy analysis of a Joule-Brayton pumped thermal electricity storage system with liquid-phase storage, Energy Conversion and Management 231 (2021) 113867. doi:10.1016/j.enconman.2021.113867.

[26] A. V. Olympios, J. D. McTigue, P. Sapin, C. N. Markides, Pumped-Thermal Electricity Storage Based on Brayton Cycles, in: Encyclopedia of Energy Storage, Elsevier Inc., 2021. doi:10.1016/B978-0-12-819723-3.00086-X.

[27] W. Steinmann, The CHEST (Compressed Heat Energy STorage) concept for facility scale thermo mechanical energy storage, Energy 69 (2014) 543–552. doi:10.1016/j.energy.2014.03.049.

[28] M. Morandin, M. Mercangöz, J. Hemrle, F. Maréchal, D. Favrat, Thermoeconomic design optimization of a thermo-electric energy storage system based on transcritical CO2 cycles, Energy 58 (2013) 571–587. doi:10.1016/j.energy.2013.05.038.

[29] A. Koen, P. Farres-Antunez, A. J. White, Low temperature sensible PTES with Kalina cycles, in: 2nd International Workshop on Carnot Batteries, Stuttgart, 2020, pp. 1–17. doi:10.17863/CAM.63240.

[30] P. Farres-Antunez, H. Xue, A. J. White, Thermodynamic analysis and optimisation of a combined liquid air and pumped thermal energy storage cycle, Journal of Energy Storage 18 (Offshore Energy Storage) (2018) 90–102. doi:10.1016/j.est.2018.04.016.

[31] J. Howes, Concept and Development of a Pumped Heat Electricity Storage Device, Proceedings of the IEEE 100 (2) (2012) 493–503. doi:10.1109/JPROC.2011.2174529.

[32] D. Salomone-González, J. González-Ayala, A. Medina, J. M. Roco, P. L. Curto-Risso, A. Calvo Hernández, Pumped heat energy storage with liquid media: Thermodynamic assessment by a Brayton-like model, Energy Conversion and Management 226. doi:10.1016/j.enconman.2020.113540.

[33] R. B. Laughlin, Pumped thermal grid storage with heat exchange, Journal of Renewable and Sustainable Energy 9 (4) (2017) 044103. doi:10.1063/1.4994054.

[34] P. Farres-Antunez, Modelling and development of thermo-mechanical energy storage, Ph.D. thesis, University of Cambridge (2018). doi:10.17863/CAM.38056.

[35] A. Bejan, The concept of irreversibility in heat exchanger design: counterflow heat exchangers for gas-to-gas applications, Journal of Heat Transfer 99 (3) (1977) 374. doi:10.1115/1.3450705.

[36] W. Kays, A. London, Compact heat exchangers, 3rd Edition, Scientific International, New York, 1984.

[37] L. S. Dixon, C. A. Hall, Fluid Mechanics and Thermodynamics of Turbomachinery, Elsevier Science, 2010.

[38] A. S. Nagorny, N. V. Dravid, R. H. Jansen, B. H. Kenny, Design aspects of a high speed permanent magnet synchronous motor / generator for flywheel applications, 2005 IEEE International Conference on Electric Machines and Drives (2005) 635–641doi:10.1109/iemdc.2005.195790.

[39] I. H. Bell, J. Wronski, S. Quoilin, V. Lemort, Pure and Pseudo-pure Fluid Thermophysical Property Evaluation and the Open-Source Thermophysical Property Library CoolProp, Industrial & Engineering Chemistry Research 53 (2014) 2498–2508. doi:10.1021/ie4033999.

[40] Y. Zhao, J. Vidal, Potential scalability of a cost-effective purification method for MgCl2-Containing salts for next-generation concentrating solar power technologies, Solar Energy Materials and Solar Cells 215 (2020) 110663. doi:10.1016/j.solmat.2020.110663.

[41] J. McTigue, Analysis and optimisation of thermal energy storage, Ph.D. thesis, University of Cambridge (2016). doi:10.17863/CAM.7084.

[42] W. Seider, D. Lewin, J. Seader, S. Widagdo, R. Gani, K. M. Ng, Product and Process Ddesign Principles: Synthesis, Analysis, and Evaluation, 4th Edition, Wiley, 2017.

[43] W. Short, D. J. Packey, A Manual for the Economic Evaluation of Energy Efficiency and Renewable Energy Technologies, NREL Technical Report NREL/TP-462-5173.

[44] S. Georgiou, N. Shah, C. N. Markides, A thermo-economic analysis and comparison of pumped-thermal and liquid-air electricity storage systems, Applied Energy 226 (2018) 1119–1133. doi:10.1016/j.apenergy.2018.04.128.

[45] Advanced Research Projects Agency - Energy (ARPA-E), Duration addition to electricity storage (DAYS) funding opportunity announcement, No. DE-FOA-0001906 (2018).

[46] C. A. Coello Coello, G. Toscano Pulido, M. Salazar Lechuga, Handling multiple objectives with particle swarm optimization, IEEE Transactions on Evolutionary Computation 8 (3) (2004) 282–290. doi:10.4018/ijmfmp.2015010104.

[47] A. Bonk, M. Braun, V. A. Sötz, T. Bauer, Solar Salt – Pushing an old material for energy storage to a new limit, Applied Energy 262 (2020) 114535. doi:10.1016/j.apenergy.2020.114535.

[48] O. Schmidt, A. Hawkes, A. Gambhir, I. Staffell, The future cost of electrical energy storage based on experience rates, Nature Energy 2 (8) (2017) 1–8. doi:10.1038/nenergy.2017.110.

[49] Lazard, Lazard's Levelized Cost of Storage Analysis - Version 6.0.

[50] C. Augustine, N. Blair, Storage Technology Modeling Input Data Report Storage Technology Modeling Input Data Report, NREL Technical Report NREL/TP-5700-78694.
URL `https://www.nrel.gov/docs/fy21osti/78694.pdf`

[51] R. K. Shah, D. P. Sekulic, Fundamentals of heat exchanger design, John Wiley & Sons, New Jersey, 2003. doi:10.1007/BF00740254.

[52] B. Cárdenas, S. Garvey, B. Kantharaj, M. Simpson, Parametric investigation of a non-constant cross sectional area air to air heat exchanger, Applied Thermal Engineering 113 (2017) 278–289. doi:10.1016/j.applthermaleng.2016.10.209.

[53] F. Incropera, D. DeWitt, T. Bergman, A. Lavine, Fundamentals of Heat and Mass Transfer, 7th Edition, John Wiley and Sons, 2011.

[54] J. Figley, X. Sun, S. K. Mylavarapu, B. Hajek, Numerical study on thermal hydraulic performance of a Printed Circuit Heat Exchanger, Progress in Nuclear Energy 68 (2013) 89–96. doi:10.1016/j.pnucene.2013.05.003.

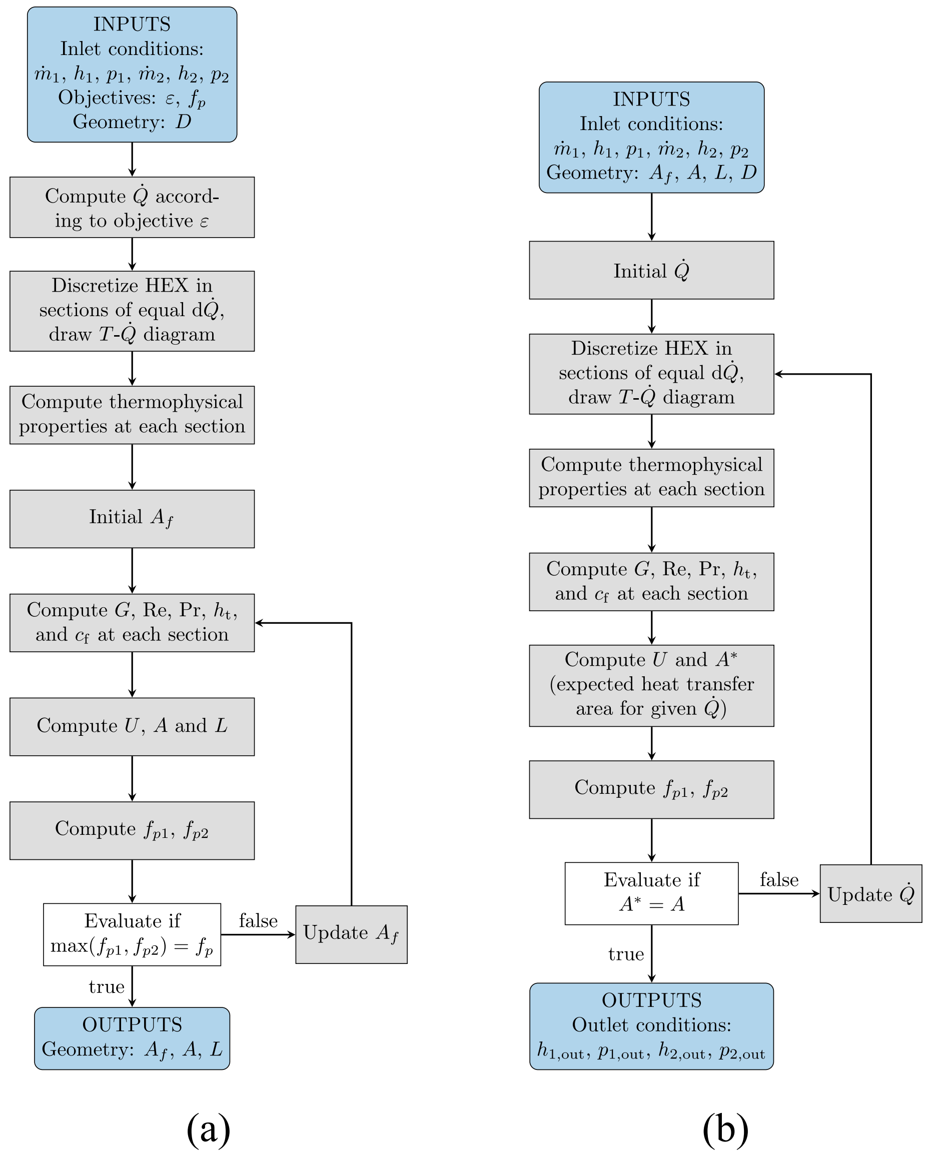

Figure A.16: Flow charts of the heat exchanger algorithms. (a) Sizing procedure. (b) Off-design model.

.

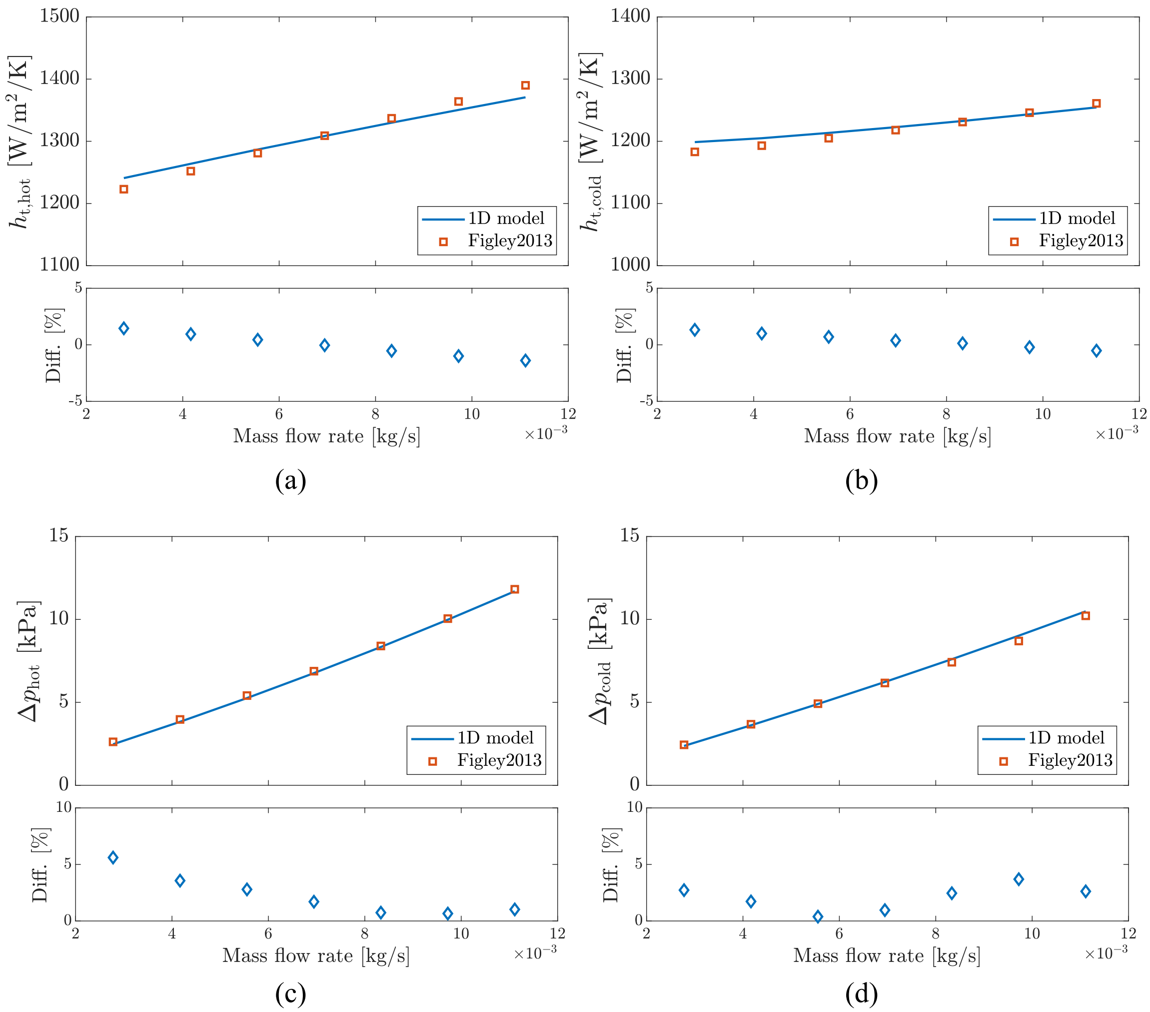

Figure A.17: Results of the one-dimensional off-design model compared to CFD simulations by Figley et al. [54]. Differences between the two are generally below $\pm 5\%$. (a) Heat transfer coefficient of the hot stream. (b) Heat transfer coefficient of the cold stream. (c) Pressure losses of the hot stream. (d) Pressure losses of the cold stream.